Supplementary Material of "**Unveiling the role of the lone electron pair in sesquioxides at high pressure: Compressibility of b-$Sb_2O_3$"**

Juan Angel Sans,[a,*] Francisco Javier Manjón,[a] André Luis de Jesus Pereira,[a,b] Javier Ruiz-Fuertes,[c] Catalin Popescu,[d] Alfonso Muñoz,[e] Plácida Rodríguez-Hernández,[e] Julio Pellicer-Porres,[f] Vanesa Paula Cuenca-Gotor,[a] Julia Contreras-García,[g] Jordi Ibañez,[h] and Virginia Monteseguro[c,f]

a) *Instituto de Diseño para la Fabricación y Producción Automatizada, MALTA Consolider Team, Universitat Politècnica de València, 46022 València, Spain*
b) *Grupo de Pesquisa em Materiais Fotonicos e Energia Renovável - MaFER, Faculdade de Ciências Exatas e Tecnologia, Universidade Federal da Grande Dourados, Dourados, Brazil*
c) *DCITIMAC, MALTA Consolider Team, Universidad de Cantabria, Santander 39005, Spain*
d) *ALBA-CELLS, 08290 Cerdanyola del Vallés, Barcelona, Spain*
e) *Departamento de Física, Instituto de Materiales y Nanotecnología, MALTA Consolider Team, Universidad de La Laguna, 38207 San Cristóbal de La Laguna, Spain*
f) *Departamento de Física Aplicada-ICMUV, MALTA-Consolider Team, Universitat de València, València, Spain*
g) *CNRS, UMR 7616, Laboratoire de Chimie Théorique, F-75005, Paris, France*
h) *Institute of Earth Sciences Jaume Almera, CSIC, 08028 Barcelona, Spain*

**Structural properties of valentinite under compression**

There are three known stable polymorphs of $Sb_2O_3$ at room conditions: $\alpha$-$Sb_2O_3$, a.k.a. mineral senarmontite **[1]**, $\beta$-$Sb_2O_3$, a.k.a. mineral valentinite **[2]**, and the recently synthesized metastable $\gamma$-$Sb_2O_3$ **[3]**. Usually, these three compounds are understood as based on trigonal $SbO_3$ units or alternatively on tetrahedral $SbO_3E$ units, where E corresponds to the lone electron pair (LEP) of Sb atoms. The three compounds show different arrangements of the above molecular units, leading to empty cavities with different geometry in each polymorph. On the one hand, $\alpha$-$Sb_2O_3$ crystallizes in a cubic phase [space group (s.g.) 227, *Fd-3m*, Z=16] and is a molecular solid composed of four distorted $SbO_3E$ units linked together by edges and forming closed adamantane-type cages ($Sb_4O_6$) arranged like carbon atoms in diamond. This polymorph is isostructural to c-$As_2O_3$ or $As_4O_6$, a.k.a. mineral arsenolite. On the other hand, $\beta$-$Sb_2O_3$ [s.g. 56, *Pccn*, Z=4] and $\gamma$-$Sb_2O_3$ [s.g. 18, $P2_12_12$, Z=8] polymorphs crystallize in orthorhombic structures which show linear channels along the *c* and *a* axes, respectively. Due to this channel-type structure, these compounds can be considered as quasi-molecular solids and it is expected that $\beta$-$Sb_2O_3$ and $\gamma$-$Sb_2O_3$ show better catalytic properties than $\alpha$-$Sb_2O_3$ just as $\beta$-$Bi_2O_3$, which also exhibit a channel-type structure, shows better catalytic properties than $\alpha$-$Bi_2O_3$ **[4]** which does not have those channels.

From a structural point of view, the orthorhombic structure of $\beta$-$Sb_2O_3$ is isostructural to $\varepsilon$-$Bi_2O_3$ and quite similar to tetragonal $\beta$-$Bi_2O_3$ also featuring empty linear cavities. The channels in all these compounds are originated by the cationic LEPs oriented towards the interior of these structural voids, providing them an outstanding stability. In $\beta$-$Sb_2O_3$, Sb LEPs point mainly along the *a*-axis leading to linear cavities running parallel to the *c*-axis, like the infinite chains or rods formed by infinite $(Sb_2O_3)_\infty$ molecules composed of linked $SbO_3E$ units. In fact, the linear voids in $\beta$-$Sb_2O_3$ are formed by alternation of LEPs corresponding to Sb atoms in opposite rods. It is worth to note that Sb atoms in $\beta$-$Sb_2O_3$ have a smaller coordination than Bi atoms in $\beta$-$Bi_2O_3$ **[5,6]**. The reason for the different coordination of cations in these two structures is the stronger activity of the LEP in Sb than in Bi, which causes a larger distortion of the electronic distribution, leading to a decrease of the coordination of the former cation despite Sb and Bi have similar ionic radii. At room pressure, the unit cell of valentinite (Fig. 1) contains two Sb4O6 units corresponding to two independents rods. Along each rod, each Sb atom is mainly linked to three O atoms forming strong Sb-O bonds of ca. 2.0 Å (see bottom of Fig. 1); thus, Sb is threefold coordinated at room pressure. As regards the O coordination, the central O of each Sb2O3 unit along the chain, hereafter named O1, is bonded to the two Sb atoms of the same unit (bond distance of 2.0 Å). Besides, it must be noted that O1 is also weakly bonded to the two Sb atoms (bond distance of 2.6 Å) of the neighbor Sb2O3 unit along the infinite chain (see oblique dashed lines in the top right part of Fig. 1). On the other hand, each of the external O atoms of each Sb2O3 unit along the chain, hereafter named O2, is bonded to a Sb atom of the same unit (bond distance of 1.98 Å) and to one Sb atom of the neighbor Sb2O3 unit (bond distance of 2.02 Å). Additionally, each O2 atom is weakly bonded (bond distance of 2.5 Å) to a Sb atom in a neighbor chain (see almost vertical dashed lines in the top part of Fig. 1). This weak bond provides the link between

the different chains or rods and leading to the formation of the 3D structure of valentinite. In summary, by taking these weak extra bonds into account, the structure of valentinite could be interpreted as formed by rods or needles with $SbO_5E$ units, where the coordination of Sb is 3 (with 2 extra-long bonds) and the coordination of O1 and O2 atoms is 2 (with 2 extra-long bonds) and 2 (with 1 extra-long bond), respectively (see the polyhedral SbO5E unit at the top part of Fig. 1).

Above 15 GPa, new Bragg reflections appear in the x-ray diffraction (XRD) pattern of β-$Sb_2O_3$ that are clear signatures of an ongoing phase transition to an unidentified HP phase. This result is in good agreement with a previous work **[7]**. We have checked that the new HP phase does not correlate with any other $Sb_2O_3$ allotrope; thus, we have searched for candidate structures among other structures observed in group-XV sesquioxides and in other antimony oxides, like $Sb_2O_4$ and $Sb_2O_5$. No clear and unambiguous identification has been found through the analysis of the XRD patterns yet. The study of the HP phase of β-$Sb_2O_3$ will be the subject of future studies.

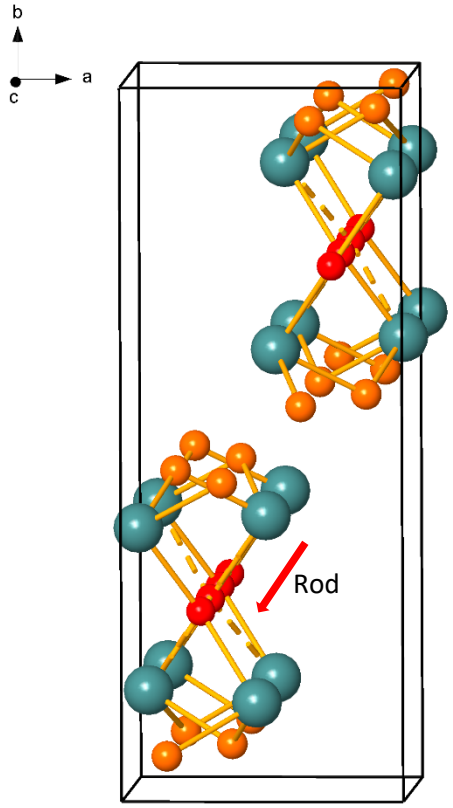


**Figure S1.** Representation of the unit cell of the valentinite compound at ambient conditions with an indication of the direction of the rod.

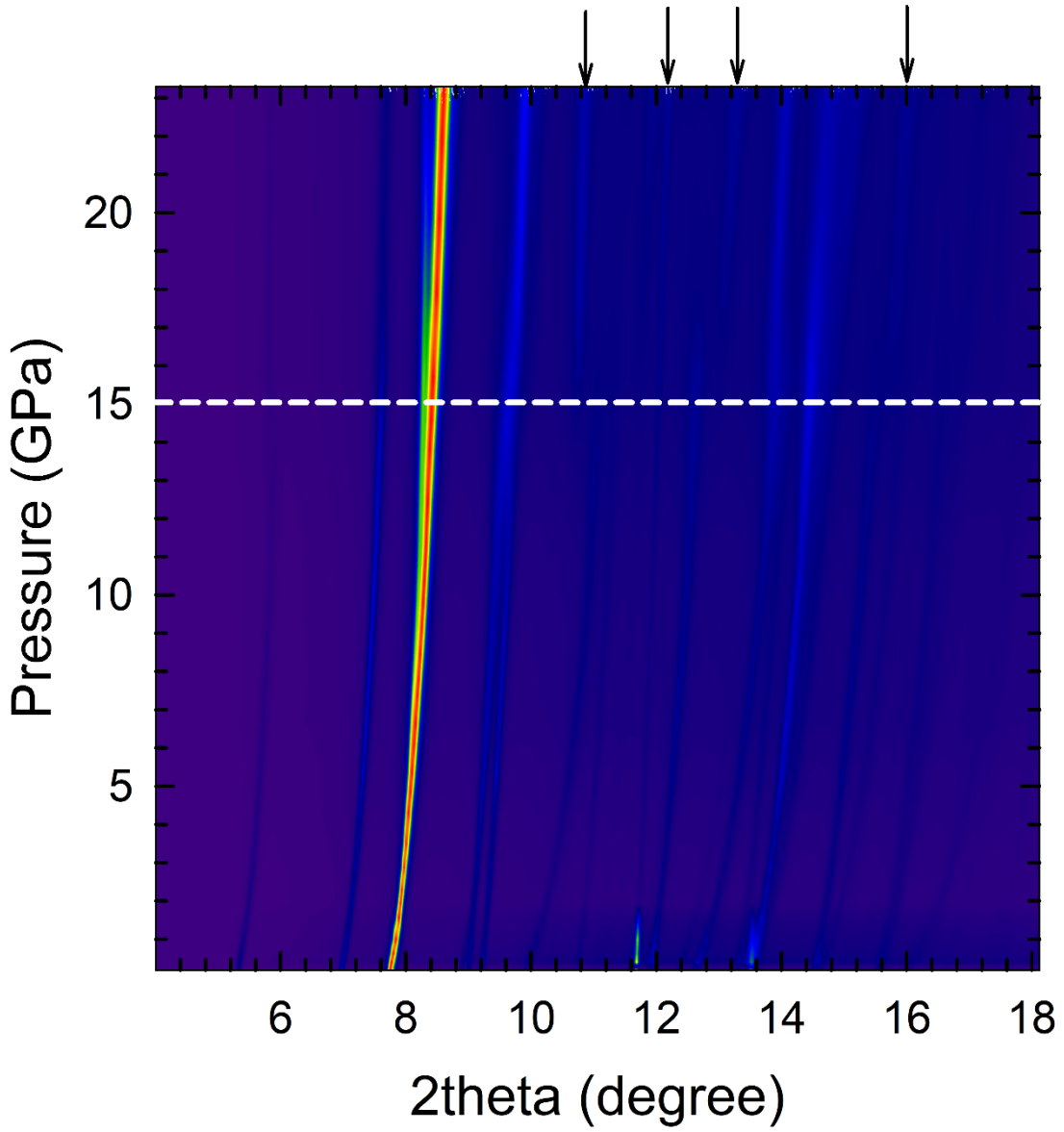


**Figure S2.** Pressure vs. 2theta color diagram showing the different contributions of the different XRD reflections of experiment 1 (with 16:3:1 methanol-ethanol-water (MEW) mixture as pressure-transmitting medium (PTM)) at each pressure. It can be observed that new reflections appear above 15 GPa.

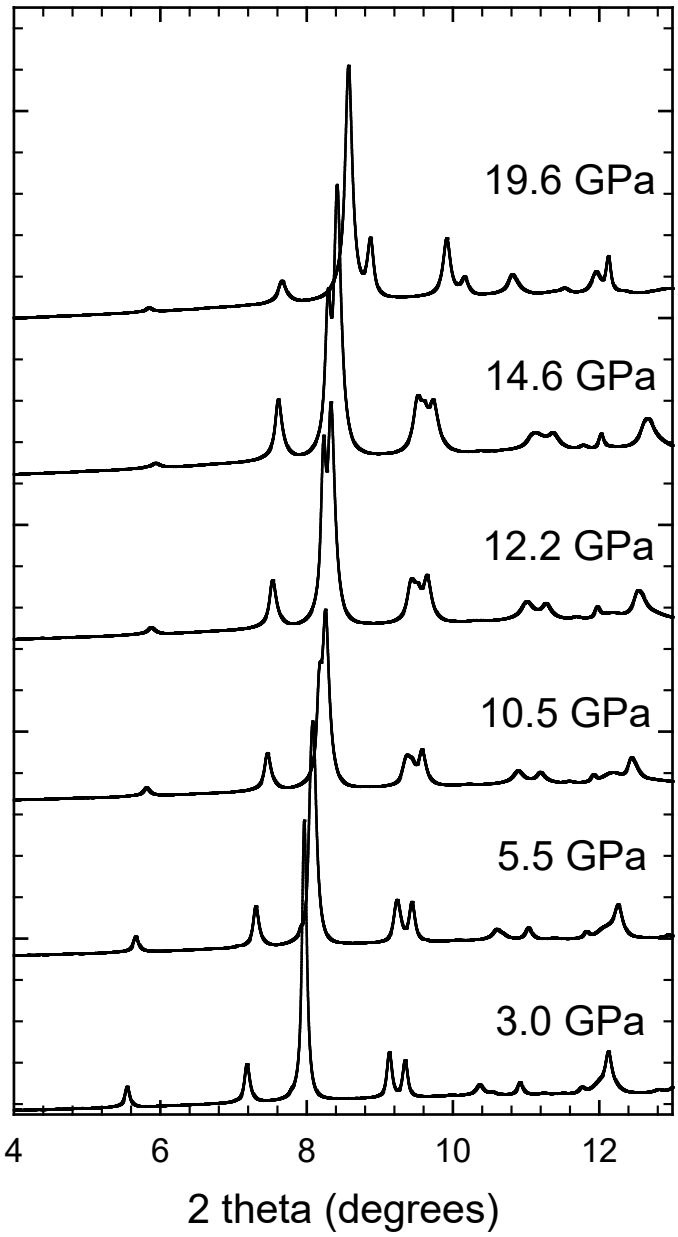


**Figure S3.** Representation of the 2-theta integrated XRD patterns of experiment 2 (with helium as a PTM) at selected pressures. Patterns are shifted for the sake of clarity.

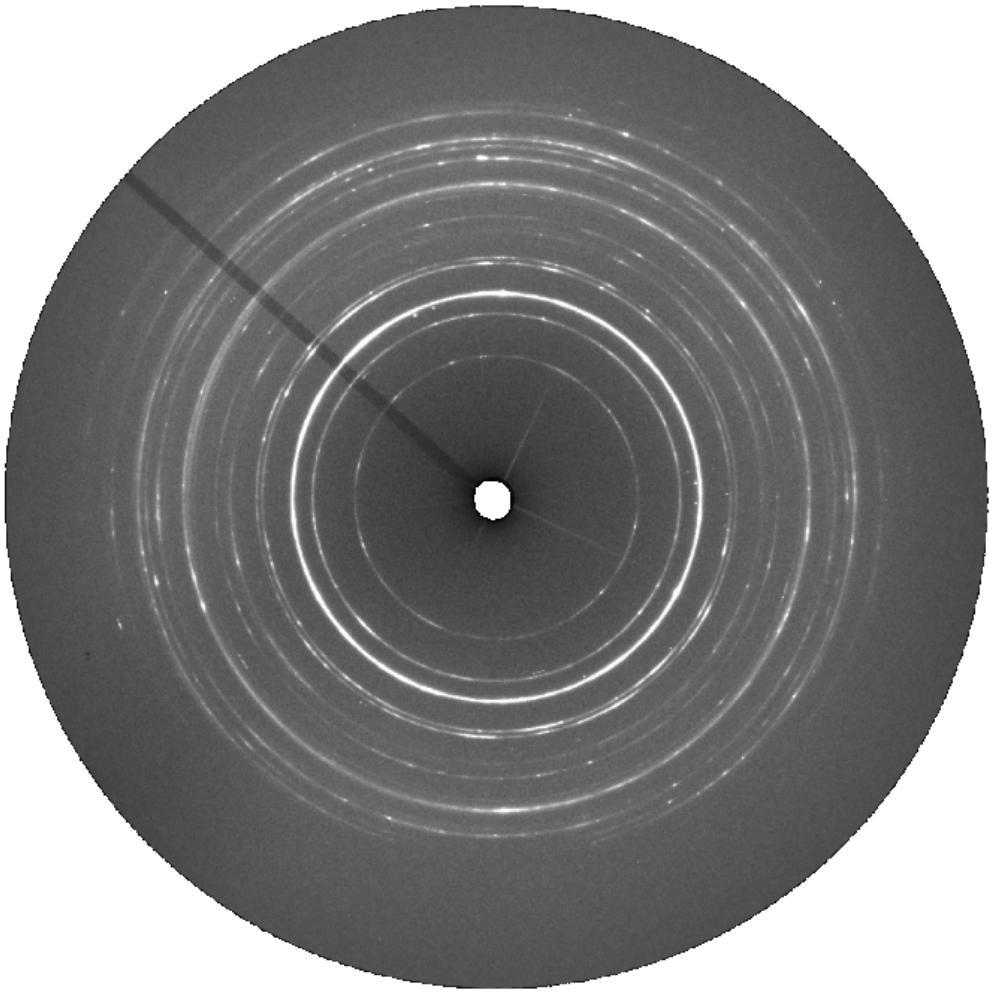

**Figure S4.** Example of 2D diffraction image of β-$Sb_2O_3$ obtained from experiment 2 at 3 GPa.

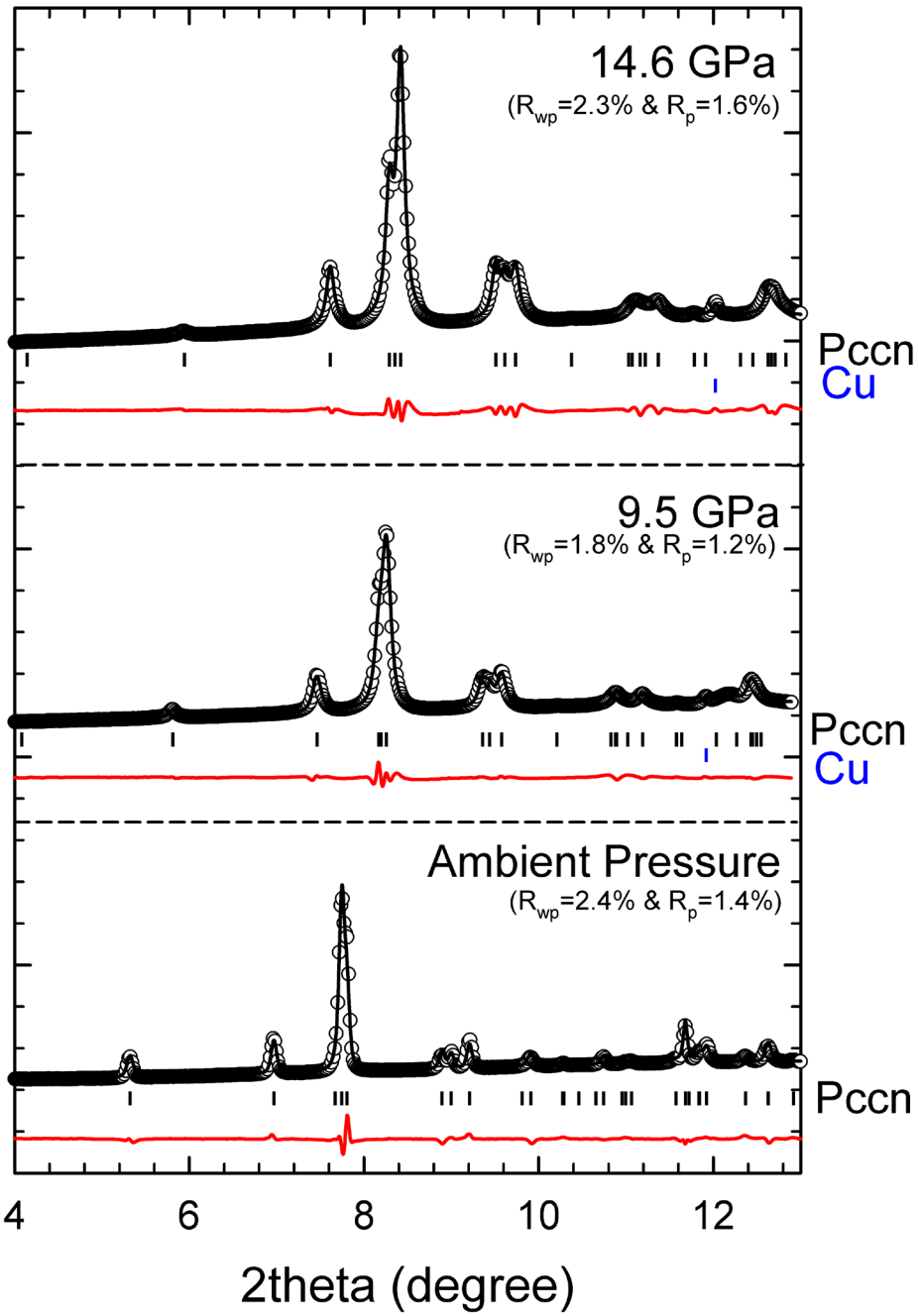


**Figure S5.** Details of XRD patterns in β-$Sb_2O_3$ at different pressures (symbols) corresponding to the experiment 2. Rietveld refinement of the XRD patterns (black line) with the *Pccn* structure is also shown. Bottom marks correspond to the peaks of the *Pccn* structure. Residuals of Rietveld refinement are also shown under each pattern (red line).

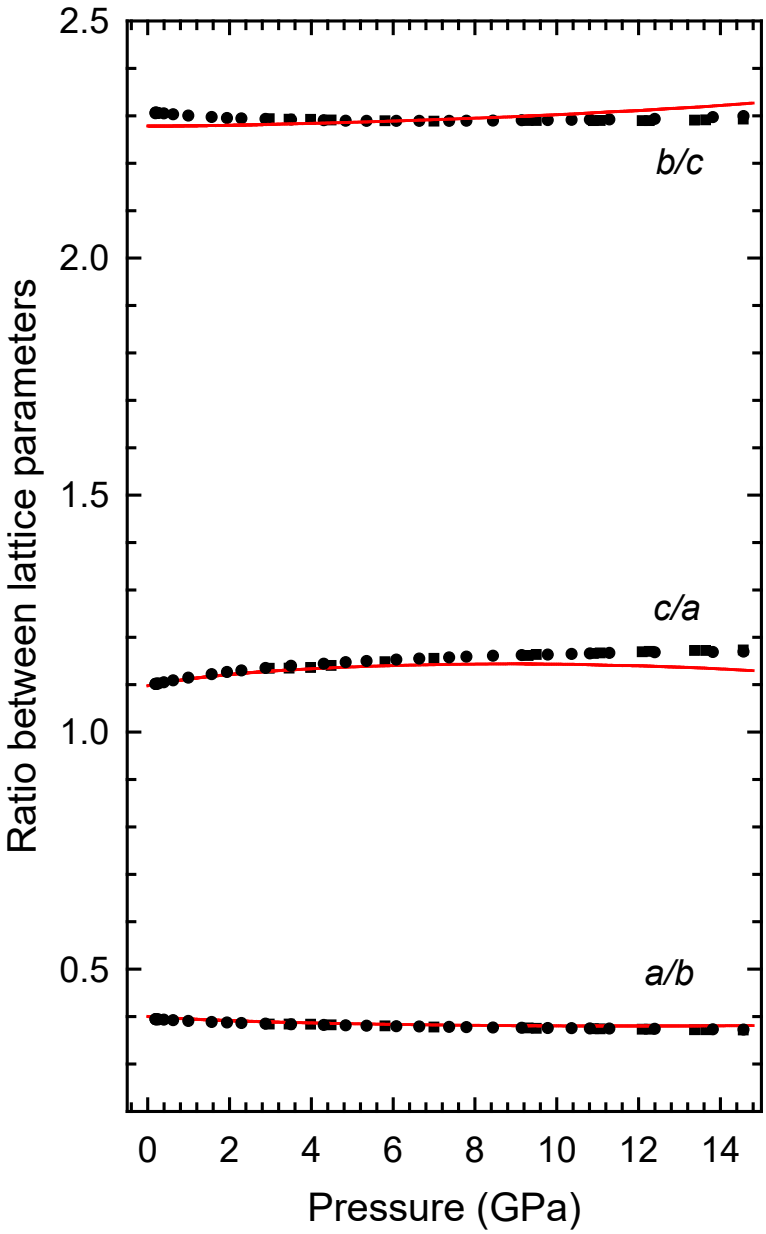


**Figure S6.** Pressure dependence of the experimental (symbols) and theoretical (lines) ratio between the lattice parameters of β-$Sb_2O_3$. Squares correspond to experiment 1 and circles to experiment 2.

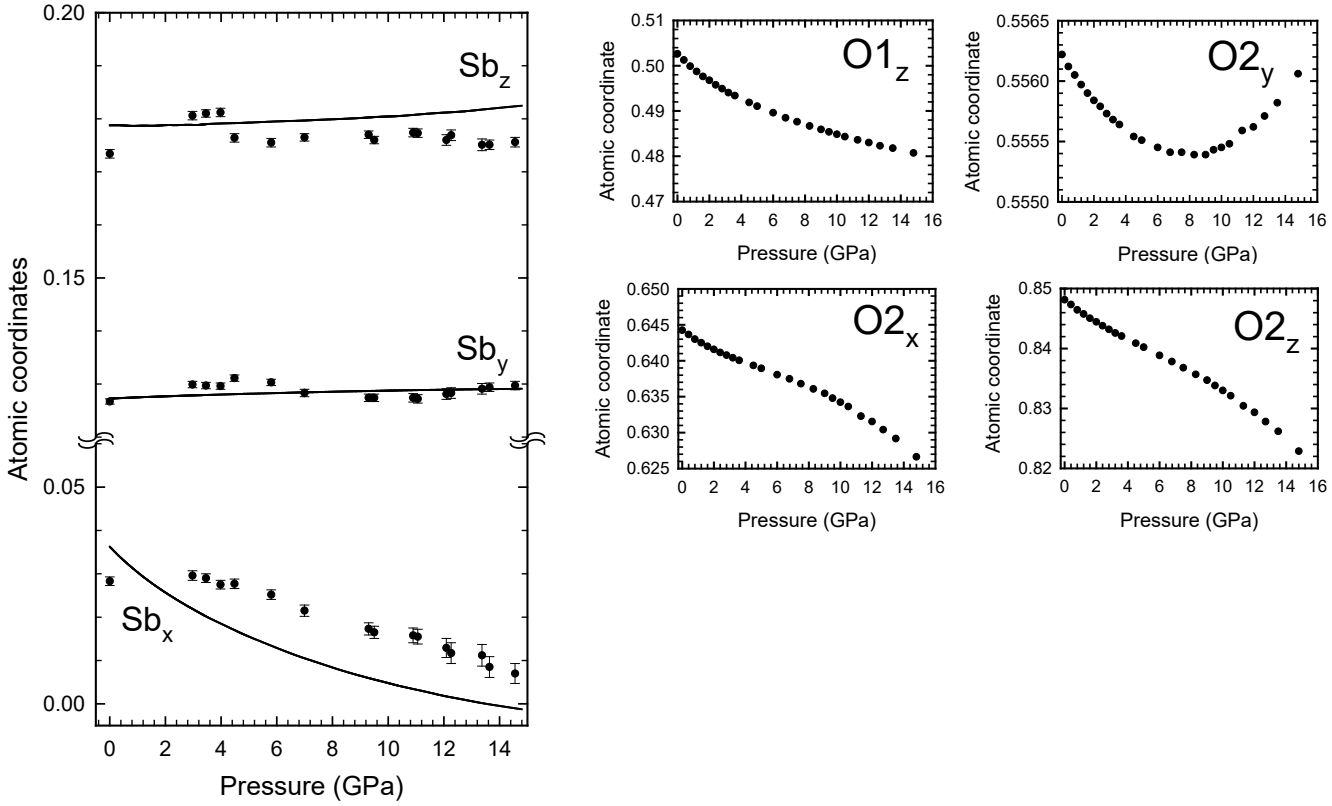


**Figure S7.** (left) Pressure dependence of the theoretical (lines) and experimental (symbols+error bars) atomic free coordinates of the Sb atom (at 8e Wyckoff position) in β-$Sb_2O_3$. Experimental data correspond to experiment 2. (right) Pressure dependence of the theoretical coordinates (symbols) of O1 (at 4c sites) and O2 (at 8e sites) atoms in β-$Sb_2O_3$.

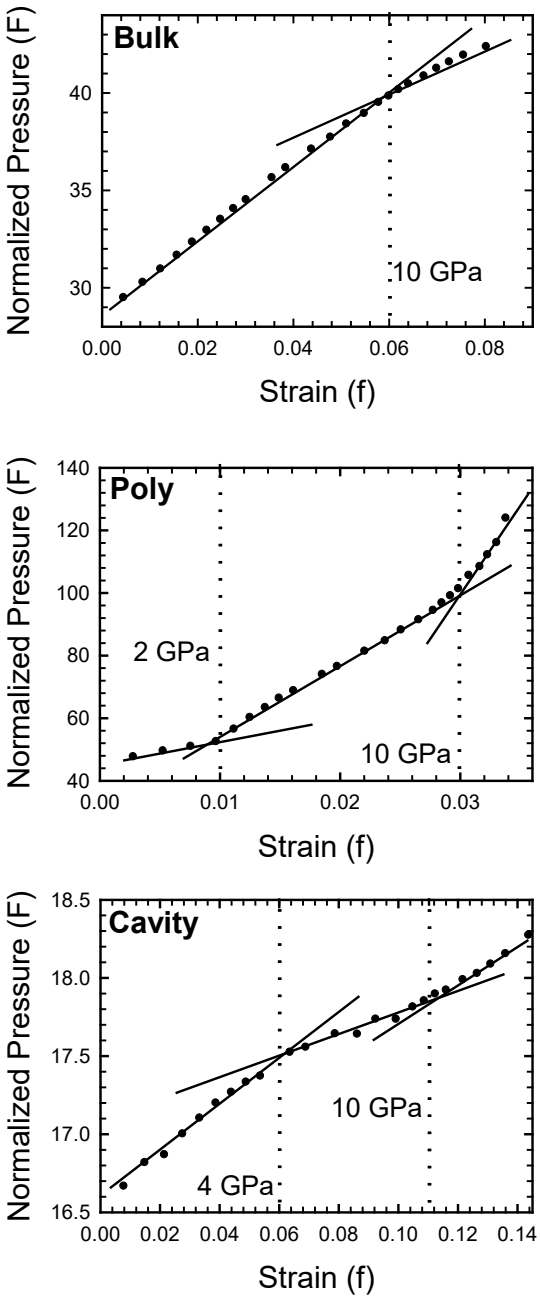


**Figure S8.** Normalized pressure vs Eulerian strain obtained from theoretical simulations for the bulk structure (top), the $SbO_5E$ polyhedron (middle) and the empty cavity (bottom). Solid lines are guidelines to define the different behavior observed and dashed lines represent the pressure at which the changes occur.

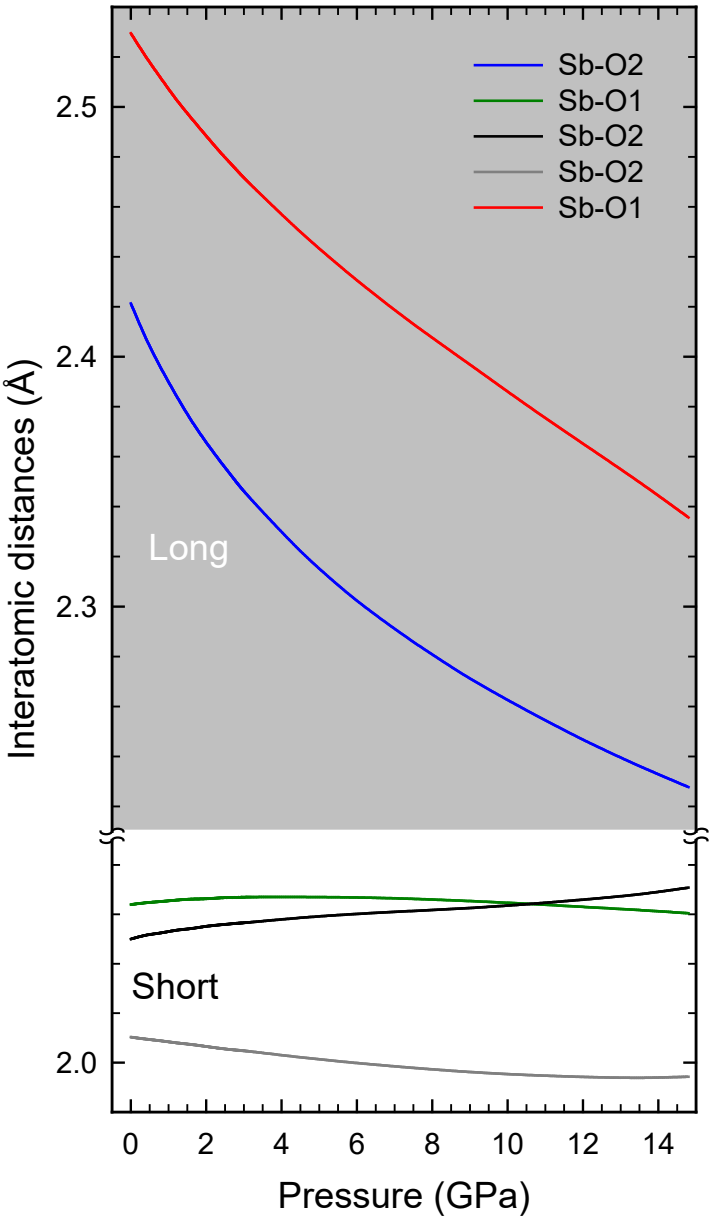


**Figure S9.** Pressure dependence of the theoretical Sb-O interatomic distances in β-$Sb_2O_3$. The three smaller Sb-O bond distances conform the $SbO_3E$ units, while taking also into account the two larger Sb-O bond distances it is possible to conform the $SbO_5E$ units mentioned in the main text. Note the slope change for the shortest Sb-O1 and second shortest Sb-O2 distances around 2 GPa and of the two short Sb-O2 distances around 10 GPa.

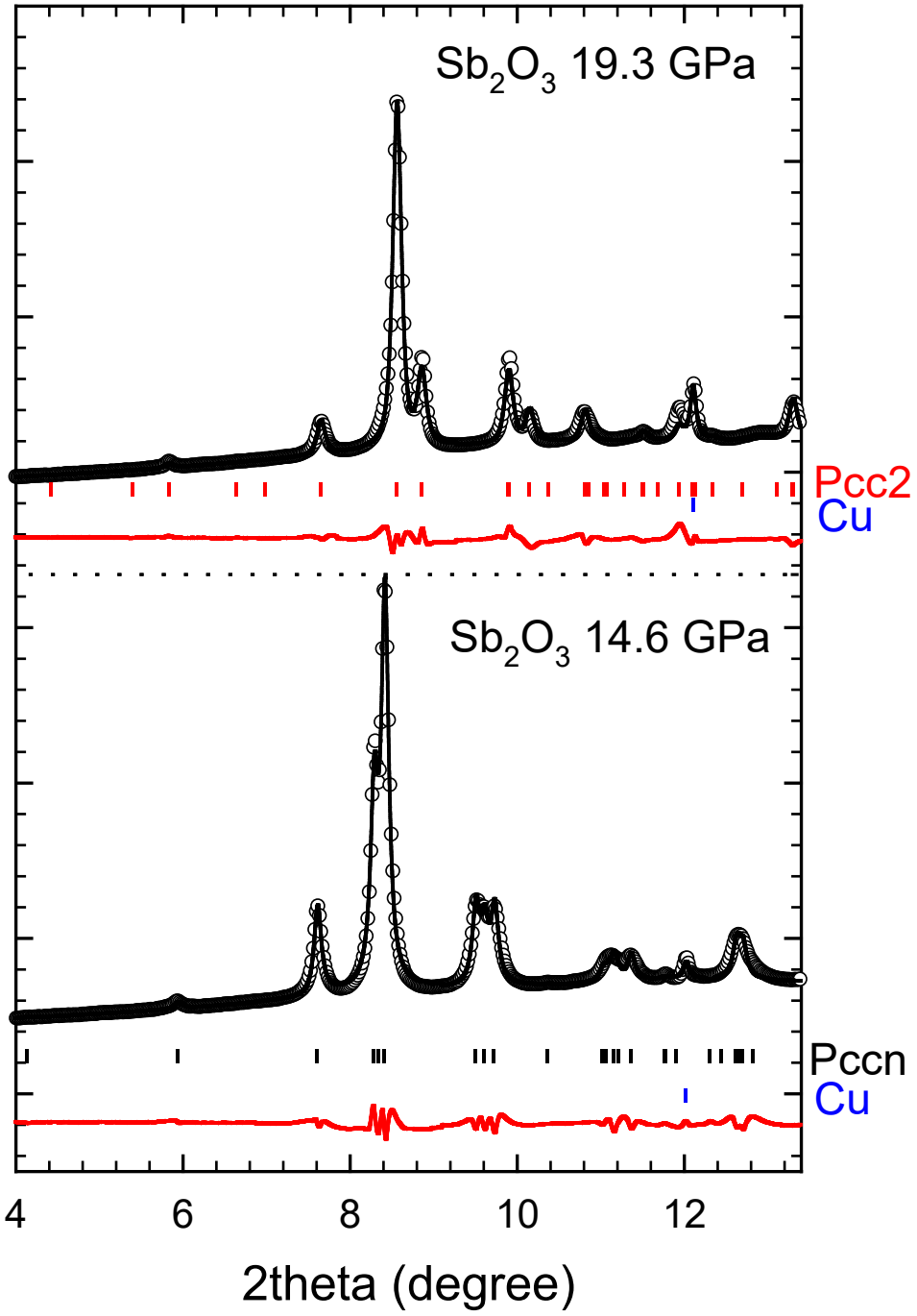


**Figure S10.** Details of XRD patterns of β-$Sb_2O_3$ corresponding to experiment 2 at pressures above (top) and below (bottom) the structural phase transition. Experimental data represented by symbols have been analyzed with a Le Bail fit (a Rietveld refinement) above (below) the phase transition and represented by black lines. Bottom marks correspond to the peaks of the *Pcc*2 (*Pccn*) structure above (below) the phase transition. Residuals of the Rietveld refinement and the Le Bail fit are also shown under each pattern (red line).

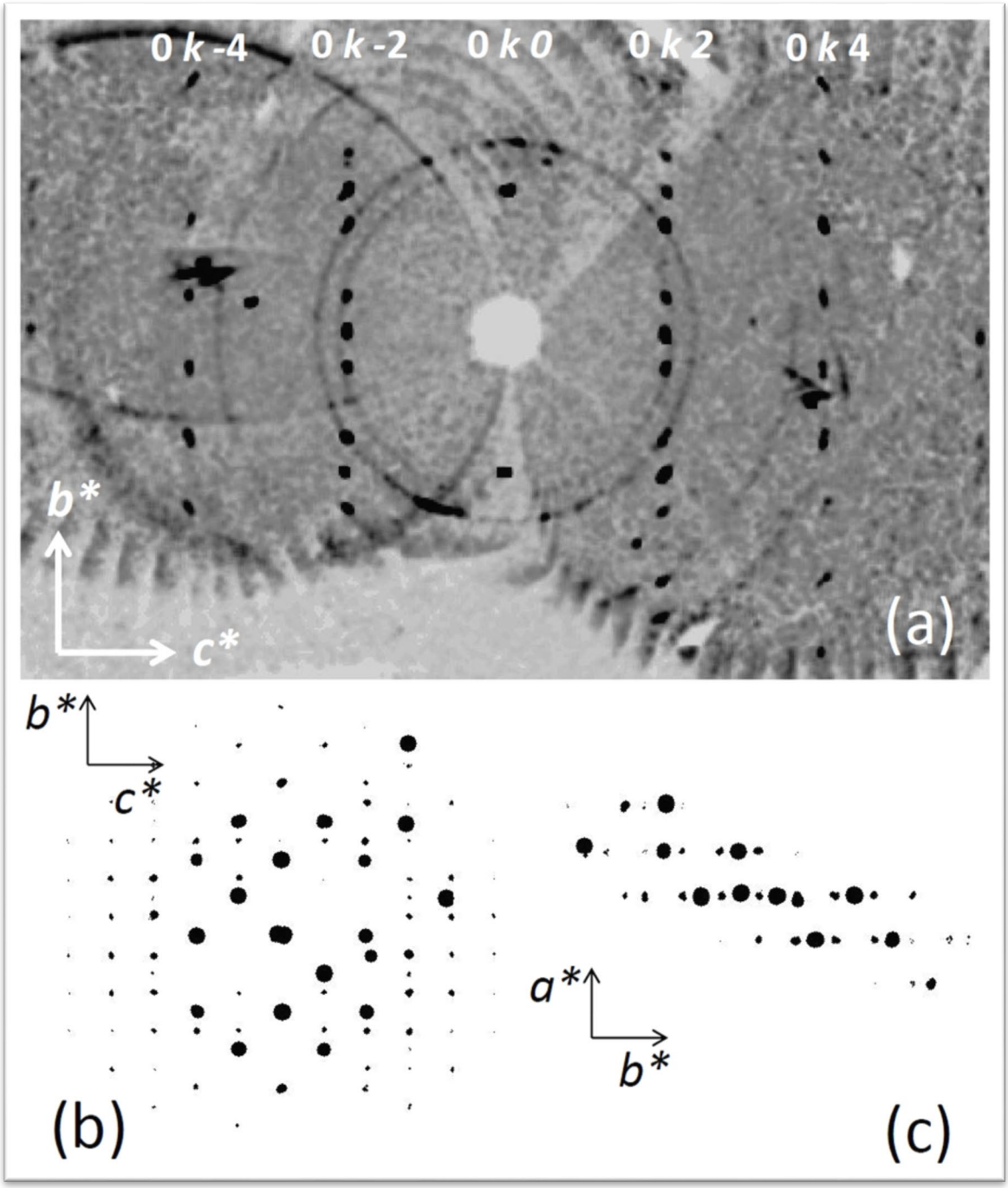


**Figure S11.** (a) Reconstruction of the accessed reciprocal space along the *b** and *c** directions at 16 GPa. The rings are due to the tungsten gasket which could not be avoided in the experiment. The variations in the background are the result of the masking applied to get rid of most of the gasket rings. (b) and (c) are the location of the measured reflections. The size of the points indicates the number of reflections collected along that direction. The orientation of the sample in the (100) translates into the reduced number of reflections along the *a** direction.

**Table S1.** Experimental and theoretical lattice and atomic parameters in valentinite at different pressures.

| Pressure (GPa) | Cell Parameters | | | Atomic positions | | | | |
|---|---|---|---|---|---|---|---|---|
| | a (Å) | b (Å) | c (Å) | Atom | x | y | z | |
| Ambient | 4.9147(7) | 12.4749(16) | 5.4122(8) | Sb (*8e*) | 0.0283(10) | 0.1267(5) | 0.1734(8) | Exp. |
| | | | | O (*8e*) | 0.147(6) | 0.097(3) | 0.820(7) | |
| | | | | O (*4c*) | 0.25 | 0.25 | 0.033(10) | |
| | 4.9017 | 12.25858 | 5.3809 | Sb (*8e*) | 0.0363 | 0.1273 | 0.1788 | Theo. |
| | | | | O (*8e*) | 0.1443 | 0.0562 | 0.8482 | |
| | | | | O (*4c*) | 0.25 | 0.25 | 0.026 | |
| 9.5 | 4.4730(5) | 11.9223(12) | 5.2059(5) | Sb (*8e*) | 0.0165(14) | 0.1274(7) | 0.1760(7) | Exp. |
| | | | | O (*8e*) | 0.1355 | 0.0554 | 0.8347 | |
| | | | | O (*4c*) | 0.25 | 0.25 | 0.0141 | |
| 9.0 | 4.5026 | 11.8349 | 5.1504 | Sb (*8e*) | 0.0065 | 0.1286 | 0.1802 | Theo. |
| | | | | O (*8e*) | 0.1355 | 0.0554 | 0.8347 | |
| | | | | O (*4c*) | 0.25 | 0.25 | 0.0141 | |
| 14.6 | 4.3660(5) | 11.7458(11) | 5.1220(5) | Sb (*8e*) | 0.0007(2) | 0.1297(8) | 0.1756(9) | Exp. |
| | | | | O (*8e*) | 0.1266 | 0.0561 | 0.8229 | |
| | | | | O (*4c*) | 0.25 | 0.25 | 0.0193 | |
| 14.8 | 4.4339 | 11.6498 | 5.0076 | Sb (*8e*) | 0.0012 | 0.1291 | 0.1825 | Theo. |
| | | | | O (*8e*) | 0.1266 | 0.0561 | 0.8229 | |
| | | | | O (*4c*) | 0.25 | 0.25 | 0.0193 | |

**Table S2.** Experimental and theoretical EOS parameters of the volume and of the axes of valentinite, including bulk modulus ($B_0$) and compressibility ($\chi$). Volume values were obtained from a fit to a third-order Birch-Murnaghan EOS and axial values were obtained from a fit to a modified Murnaghan EOS.

| | $V_0$ (Å$^3$) | $B_0$ (GPa) | $B_0'$ | $B_{0a}$ (GPa) | $\chi_a$ ($10^{-3}$) | $B_{0b}$ (GPa) | $\chi_b$ ($10^{-3}$) | $B_{0c}$ (GPa) | $\chi_c$ ($10^{-3}$) |
|---|---|---|---|---|---|---|---|---|---|
| Experiment 1 (MEW) | 332.7(12) | 27.4(8) | 7.4 | 12.4(16) | 26.9(12) | 40(2) | 8.3(14) | 76(4) | 4.38(8) |
| Experiment 2 (He) | 338(5) | 24(2) | 7.4 | 21(6) | 15.9(15) | 50(9) | 6.7(4) | 72(10) | 4.6(2) |
| Unified EoS (Exp. 1+2) | 334.0(11) | 27(2) | 7.4 | 14.3(6) | 23.3(9) | 41(2) | 8.1(4) | 61(2) | 5.5(2) |
| Theoretical simulation | 322.8(2) | 30.9(5) | 7.4(2) | 13.6(5) | 24.5(9) | 59(1) | 5.65(3) | 62.7(17) | 5.3(4) |

**Table S3.** Experimental and theoretical lattice and atomic parameters for the high pressure phase of β-$Sb_2O_3$. In red, unreliable values of the oxygen atomic site obtained by single-crystal XRD.

| | Cell Parameters | | | Atomic positions | | | |
|---|---|---|---|---|---|---|---|
| | **a (Å)** | **b (Å)** | **c (Å)** | **Atom** | **x** | **y** | **z** |
| **Theoretical calculations (24.6 GPa)** | 4.416 | 11.521 | 4.868 | Sb1 (*4e*) | 0.243820 | 0.37938 | 0.15983 |
| | | | | Sb2 (*4e*) | 0.25619 | 0.12065 | 0.791 |
| | | | | O1 (*2c*) | 0.5 | 0 | 0.54839 |
| | | | | O2 (*2b*) | 0 | 0.5 | 0.09927 |
| | | | | O3 (*4e*) | 0.36436 | 0.19267 | 0.7196 |
| | | | | O4 (*4e*) | 0.1355 | 0.30726 | 0.32836 |
| **Single-crystal XRD (17.8 GPa)** | 4.590(14) | 11.113(7) | 4.9730(16) | Sb1 (*4e*) | 0.24635 | 0.37236 | 0.16781 |
| | | | | Sb2 (*4e*) | 0.26043 | 0.12922 | 0.7856 |
| | | | | O1 (*2c*) | 0.5 | 0 | 0.67847 |
| | | | | O2 (*2b*) | 0 | 0.5 | 0 |
| | | | | O3 (*4e*) | 0.2905 | 0.09767 | 0.5780 |
| | | | | O4 (*4e*) | 0.13235 | 0.29617 | 0.4038 |
| **Powder XRD (19.3 GPa)** | 4.2690(15) | 12.087(6) | 4.8396(15) | Sb1 (*4e*) | 0.24129 | 0.37947 | 0.16106 |
| | | | | Sb2 (*4e*) | 0.25871 | 0.12053 | 0.78772 |
| | | | | O1 (2c) | 0.5 | 0 | 0.54829 |
| | | | | O2 (*2b*) | 0 | 0.5 | 0.09951 |
| | | | | O3 (*4e*) | 0.36252 | 0.19275 | 0.87361 |
| | | | | O4 (4e) | 0.13748 | 0.30724 | 0.27419 |

**Lattice dynamics of valentinite at room pressure**

Regarding the vibrational properties of antimony oxides, they have been extensively studied by Raman scattering (RS) in $\alpha$-$Sb_2O_3$ **[8-10]**, the cubic phase present in mineral senarmontite, with an accurate approach to the symmetry of their Raman modes and their evolution with pressure **[11]**. However, the symmetry of the Raman-active modes in $\beta$-$Sb_2O_3$, the orthorhombic phase present in mineral valentinite, is more complex and has not been clearly assigned in the literature despite RS measurements have been provided in a number of works **[12-16]**. In fact, HP-RS measurements recently published **[7,17]** have provided tentative assignments of the symmetry of the vibrational modes; however, they have failed because vibrational modes have been interpreted in terms of the molecular $Sb_4O_6$ units present in senarmontite, but not in terms of the infinite $(Sb_2O_3)_\infty$ molecules present in valentinite **[10]**. A better approach to interpret the RS and infrared (IR) spectra of valentinite has been performed by Voit *et al.*, who used $Sb_{10}O_{15}$ units to model vibrational spectra **[18]**. In the following, we will assign the symmetry of the experimentally observed first-order Raman-active modes of $\beta$-$Sb_2O_3$ and their pressure dependences with the help of theoretical lattice-dynamics *ab initio* calculations.

According to group theory **[19]**, the orthorhombic phase of $\beta$-$Sb_2O_3$ with $D_{2h}$ (mmm) point group should have 60 zone-center phonon modes belonging to the following irreducible representation: $\Gamma_{60} = 7A_g + 7A_u + 7B_{1g} + 7B_{1u} + 8B_{2g} + 8B_{2u} + 8B_{3g} + 8B_{3u}$. Three of these modes ($B_{1u}$, $B_{2u}$, and $B_{3u}$) correspond to acoustic phonons, while $A_u$ modes are silent modes. This results in 30 Raman-active (gerade) optical modes ($7A_g + 7B_{1g} + 8B_{2g} + 8B_{3g}$) and 20 IR-active (ungerade) optical modes ($6B_{1u} + 7B_{2u} + 7B_{3u}$). In the following, all optical modes are numbered with a superindex in order of increasing frequency.

We have visualized atomic movements of all vibrational modes in valentinite thanks to the J-ICE software **[20]** and here we provide pictures of several modes taken with it. The most intense Raman mode is attributed to the $B_{1g}^2$ mode (near 140 $cm^{-1}$). Noteworthy, the Raman-active $B_{1g}^2$ and IR-active $B_{1u}^1$ modes (both slightly below 140 $cm^{-1}$) correspond to antisymmetric and symmetric vibrations of Sb atoms along the *b* axis with respect to central O1 atoms located at the two-fold axis (see **Figure S12**).

Other low-frequency modes, where there is an important movement of Sb atoms, are IR-active in $B_{2u}^1$ (25 $cm^{-1}$) and Raman-active $A_g^1$ (75 $cm^{-1}$) modes, respectively, which correspond to antisymmetric and symmetric vibrations of Sb atoms mainly along the *c* axis (see left part of **Figure S13**). On the other hand, examples of middle frequency modes with dominant movement of central O1 atoms are the antisymmetric and symmetric vibrations of these atoms mainly along the *c* axis in $A_g^5$ (301 $cm^{-1}$) and $B_{1u}^4$ (322 $cm^{-1}$) modes, respectively (see right part of **Figure S13**).

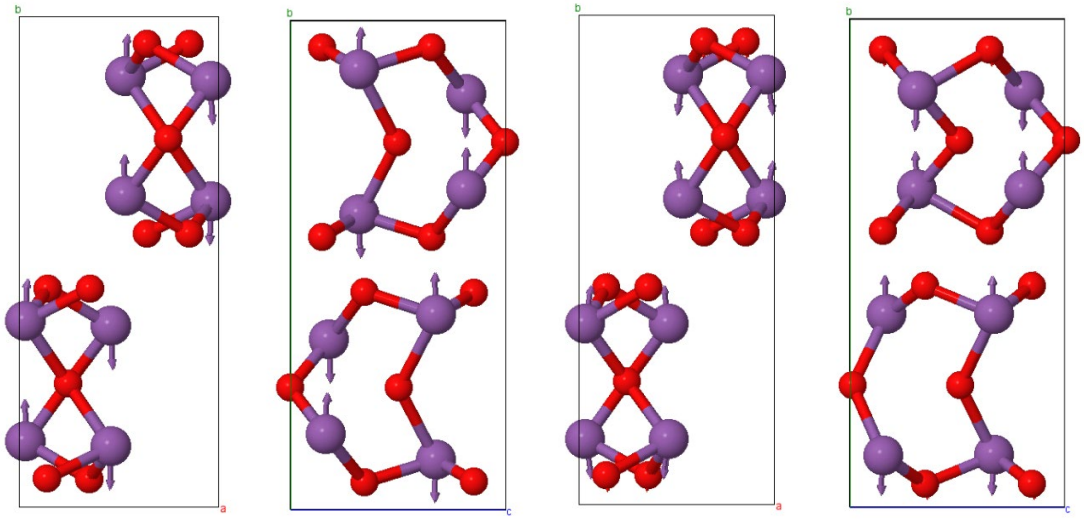

**Figure S12**. Antisymmetric and symmetric atomic movements of Sb atoms along the *b* axis in $B_{1g}^{2}$ (two left figures) and $B_{1u}^{1}$ (two right figures) modes close to 140 $cm^{-1}$, respectively. Two different rods (up and down) extending along the b axis are plotted inside the unit cell, like in Figure S1. Sb atoms are depicted in purple color and O atoms in red color.

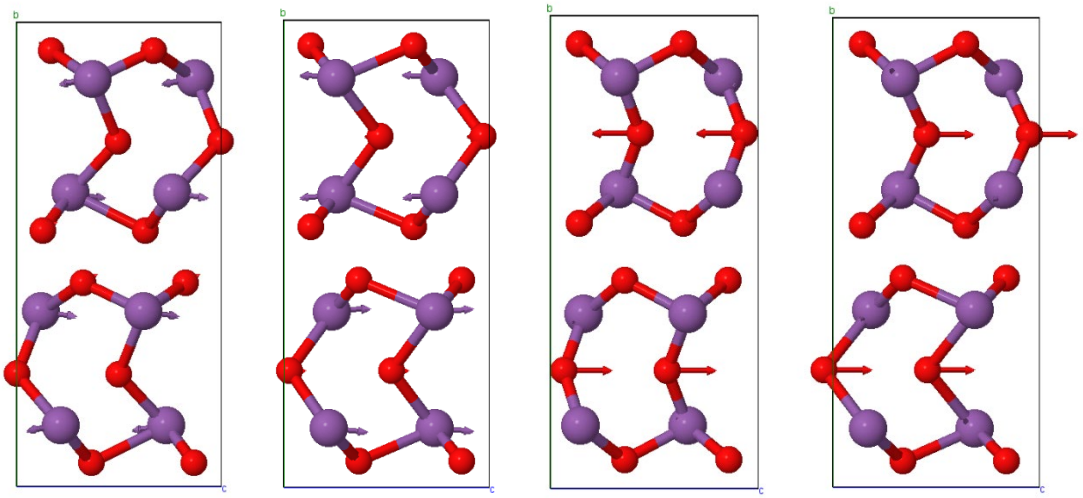

**Figure S13**. Left part: Antisymmetric and symmetric vibrations of Sb atoms mainly along the *c* axis in $B_{2u}^{1}$ (25 $cm^{-1}$) and $A_{g}^{1}$ (75 $cm^{-1}$) modes, respectively, as viewed in the *bc* plane. Right part: antisymmetric and symmetric vibrations of central O1 atoms mainly along the *c* axis in $A_{g}^{5}$ (301 $cm^{-1}$) and $B_{1u}^{4}$ (322 $cm^{-1}$) modes, respectively, as viewed in the *bc* plane. Sb atoms are depicted in purple color and O atoms in red color.

Finally, examples of high-frequency modes, where movement of O atoms is clearly dominant, are $B_{2g}^{7}$ (577 $cm^{-1}$), $B_{2u}^{7}$ (642 $cm^{-1}$) and $B_{3g}^{8}$ (659 $cm^{-1}$) modes, which correspond to atomic movements of central O1 atoms against the Sb atoms mainly along the *b* axis (see **Figure S14**).

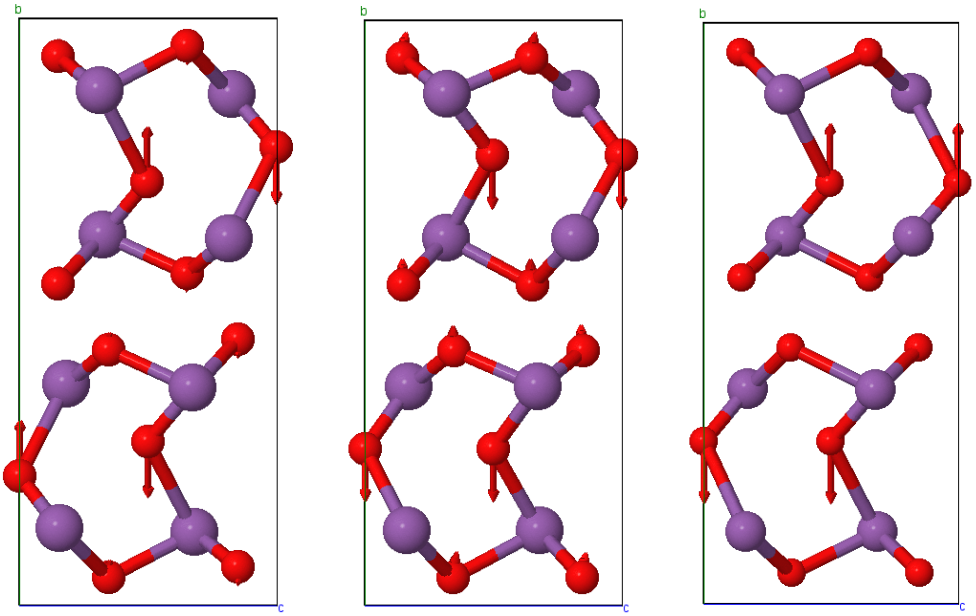

**Figure S14**. From left to right: Atomic movements of central O1 atoms against the Sb atoms along the *b* axis in $B_{2g}^{7}$ (577 $cm^{-1}$), $B_{2u}^{7}$ (642 $cm^{-1}$) and $B_{3g}^{8}$ (659 $cm^{-1}$) modes, respectively, as seen in the *bc* plane.

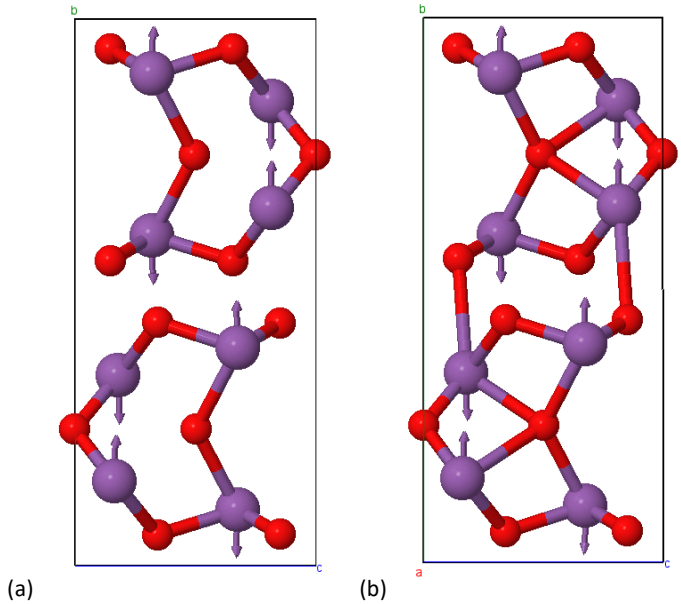

(a) (b)

**Figure S15**. *bc* plane: Atomic movements in the $B_{1g}^{2}$ mode (near 140 $cm^{-1}$) which softens above 2 GPa: (a) below 2 GPa, (b) above 2 GPa. Note that inter-rod and intra-rod Sb-O bonds are included above 2 GPa in order to emphasize the importance of these interactions above 2 GPa. In this mode, the main movement of Sb atoms is along the *c* axis and it is strongly influenced by the inter-rod bonds mainly directed along the *c* axis.

The atomic vibrations of other modes are exemplified in **Figs. S16 to S20**.

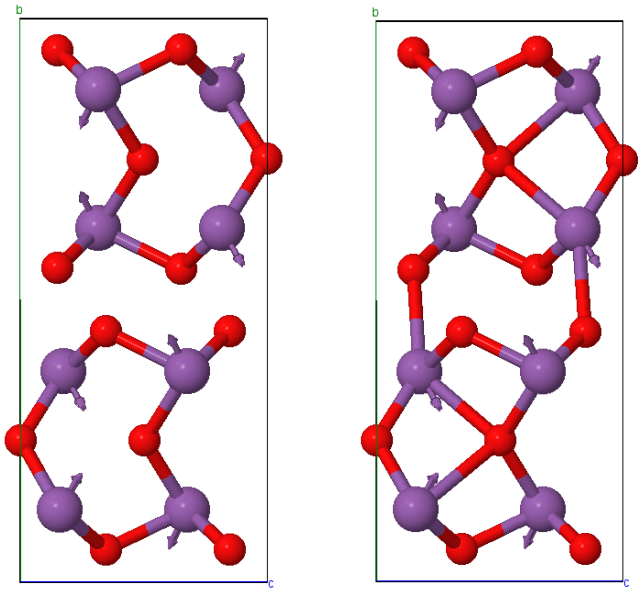


(a) (b)

**Figure S16**. *bc* plane: Atomic movements in the $A_u^2$ mode (97 $cm^{-1}$): (a) below 2 GPa, (b) above 2 GPa, where inter-rod and intra-rod Sb-O bonds are included. In this mode, Sb atoms vibrate against the central O1 atom, so this mode changes the slope around 2 GPa and hardens with increasing pressure once inter and intra-rod bonds are considered.

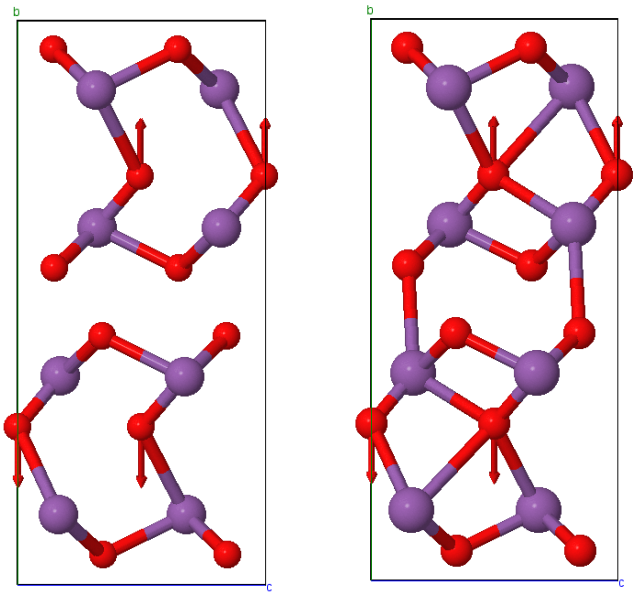


(a) (b)

**Figure S17**. *bc* plane: Movements of central O1 atoms against Sb atoms in the $B_{3g}^8$ mode (659 $cm^{-1}$): (a) below 2 GPa, (b) above 2 GPa, where inter-rod and intra-rod Sb-O bonds are included. This mode also changes slope around 2 GPa and hardens considerably with increasing pressure once inter-rod and intra-rod bonds are considered. In this mode, the vibration of central O1 atom is clearly influenced by the intra-rod Sb-O1 bonds.

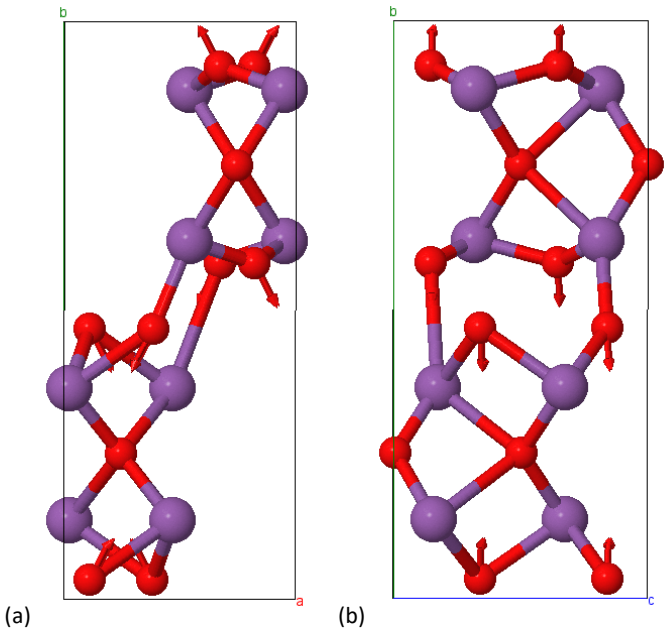


**Figure S18**. Atomic movements in the $B_{1u}^{6}$ mode (578 $cm^{-1}$), as viewed in the *ab* plane (a) and in the *bc* plane (b). This mode strongly hardens with increasing pressure (it is the vibrational mode with highest pressure coefficient), but also strongly softens above 14 GPa (close to the observed pressure-induced first-order phase transition), thus suggesting a softening or break of interatomic links related to external O2 atoms.

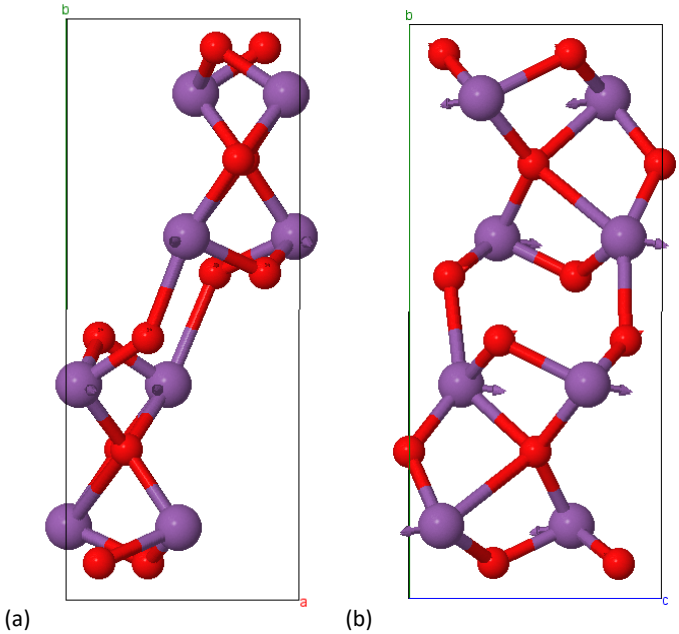


**Figure S19**. Atomic movements in the $B_{2u}^{1}$ mode (25 $cm^{-1}$). This mode strongly softens above 10 GPa and has a minimum value near 14 GPa, close to the pressure-induced first-order phase transition.

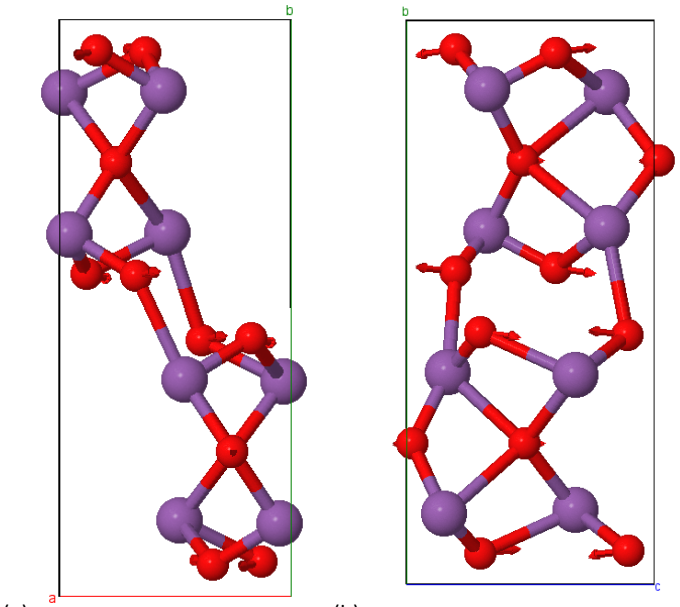


**Figure S20**. Atomic movements in the $A_u^7$ mode (592 $cm^{-1}$). This mode strongly hardens above 10 GPa, thus reflecting the strong interaction between neighboring rods in this pressure range.

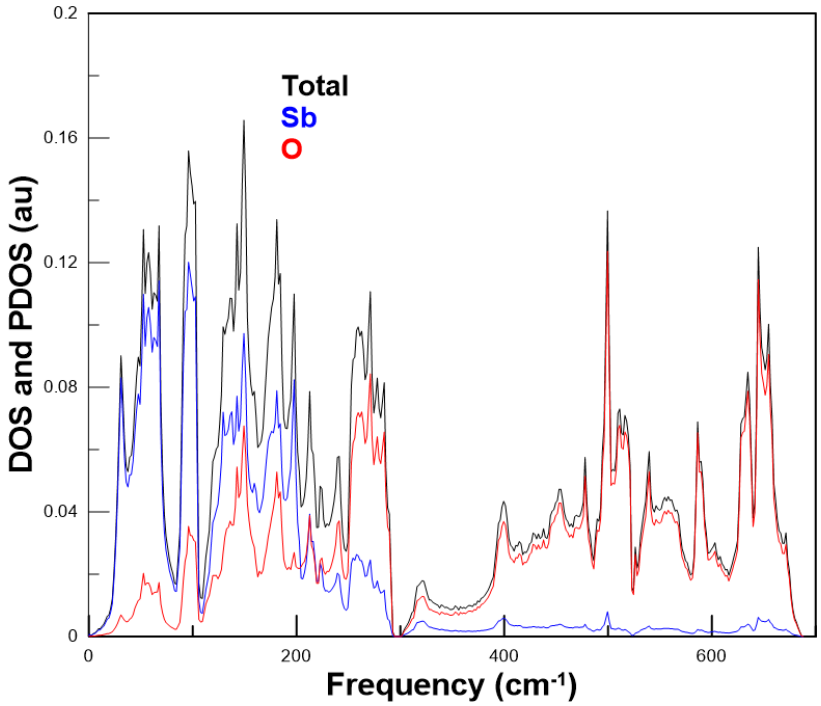


**Figure S21**. Partial (Sb and O) and total phonon density of states of β-$Sb_2O_3$ at room pressure. There is a strong contribution of Sb atoms to the low-frequency vibrational modes below 100 $cm^{-1}$, a mixed contribution of Sb and O atoms to the middle-frequency vibrational modes between 100 and 300 $cm^{-1}$, and a strong contribution of O atoms to the high-frequency vibrational modes above 300 $cm^{-1}$.

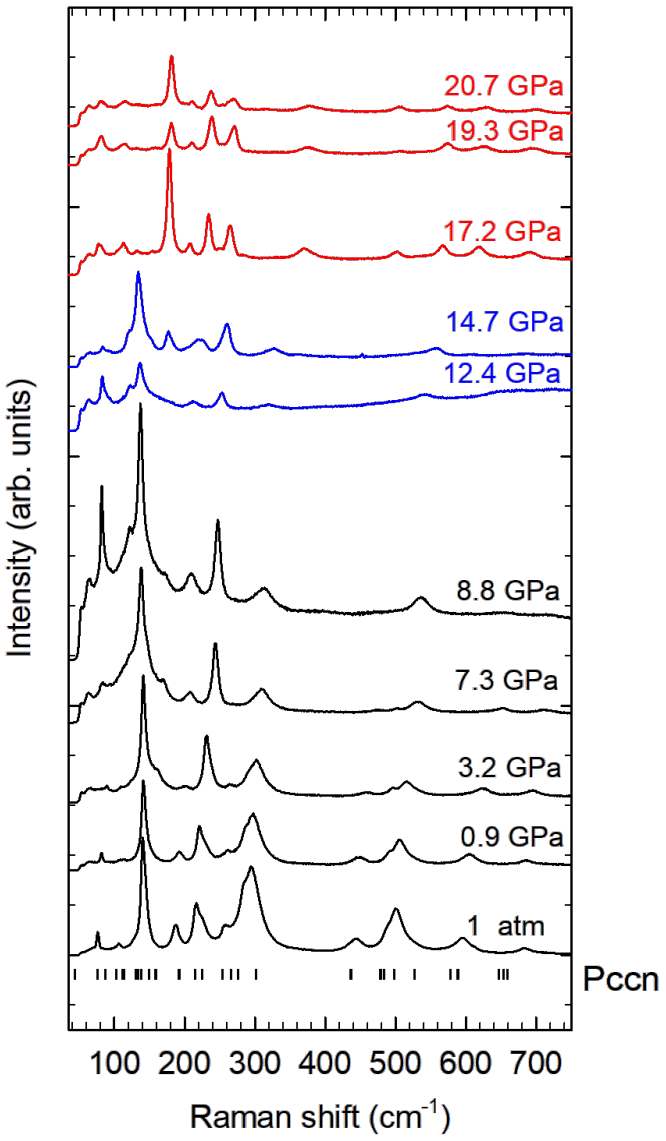


**Figure S22.** Selected RS spectra of powder β-$Sb_2O_3$ at different pressures on upstroke up to 20.7 GPa. Spectra are vertically shifted for the sake of clarity. Ticks at the bottom represent the theoretical frequencies of Raman-active modes of β-$Sb_2O_3$ at room pressure from our *ab-initio* calculations. A notable decrease in Raman intensity of the modes of the low-pressure phase is observed above 10 GPa.

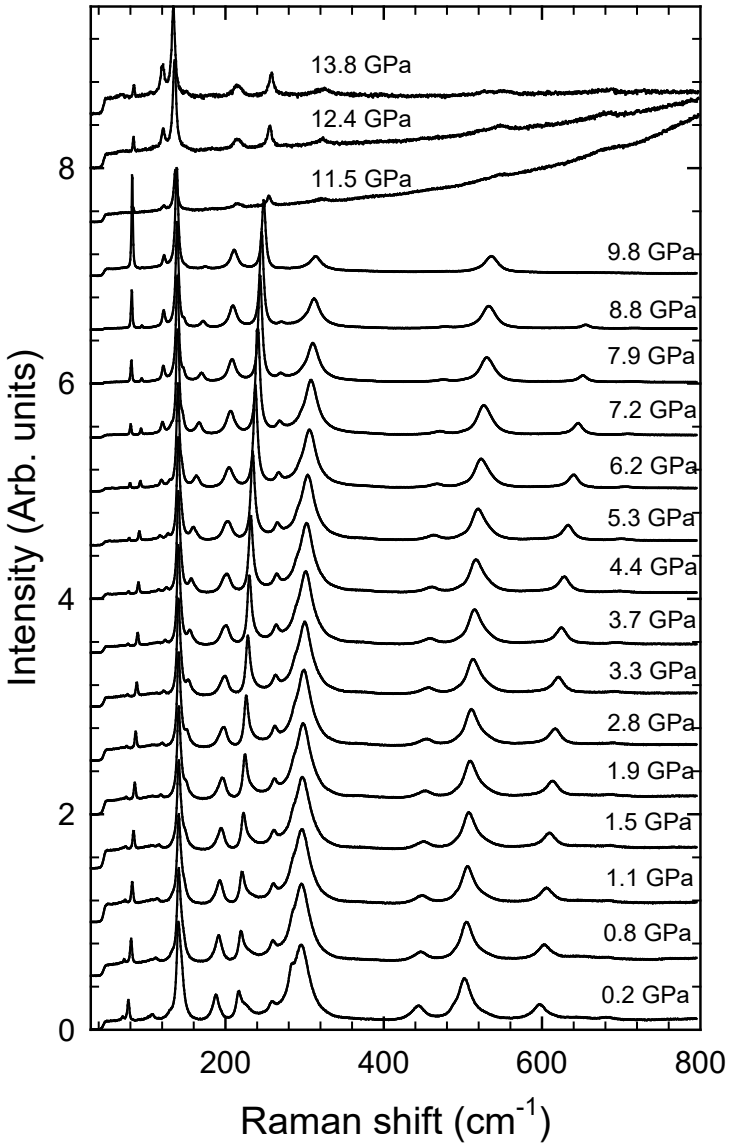


**Figure S23.** Selected RS spectra of single-crystal β-$Sb_2O_3$ at different pressures on upstroke up to 13.8 GPa. Spectra are vertically shifted for the sake of clarity. Above 10 GPa, similar decrease of the Raman intensity as in the powder sample has been observed.

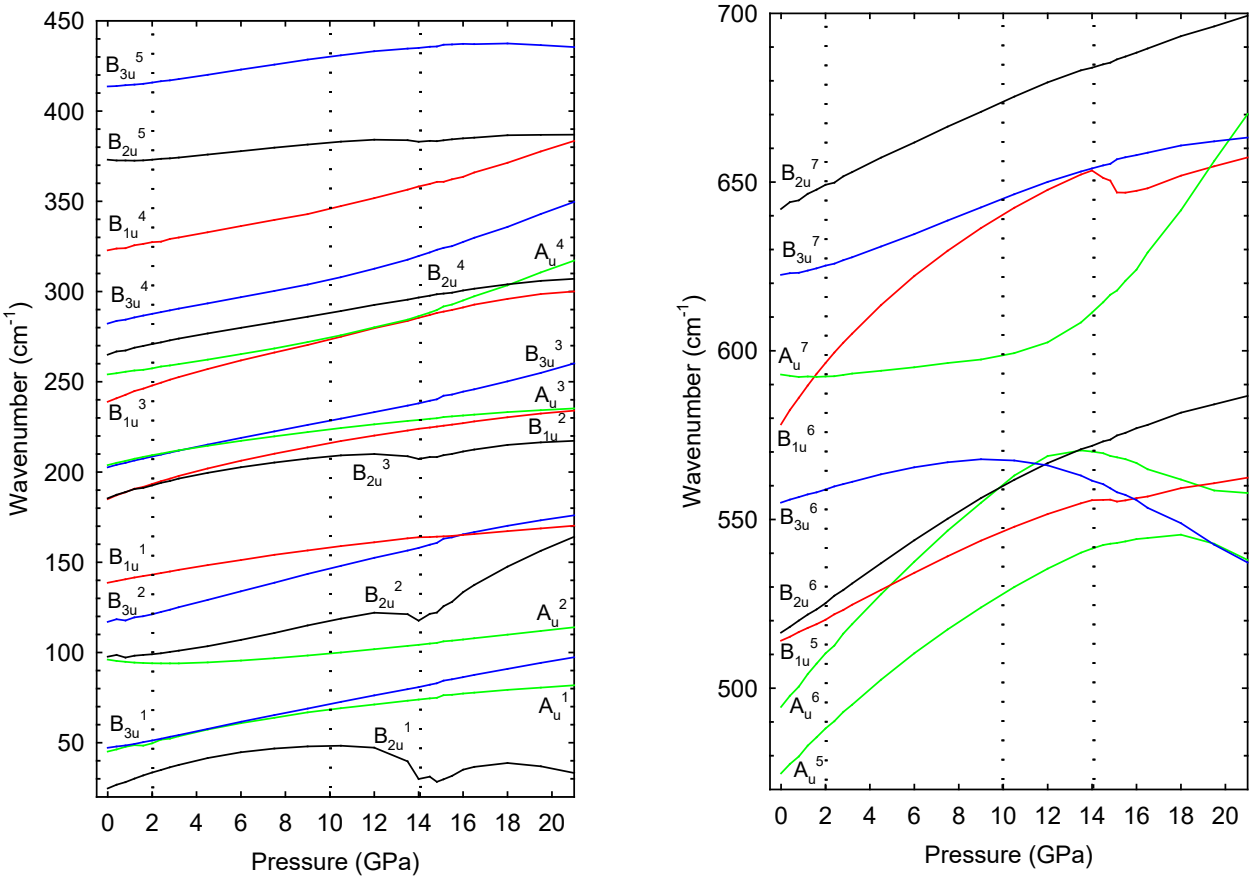


**Figure S24.** Pressure dependence of the theoretical infrared-active and silent vibrational modes of β-$Sb_2O_3$ below 450 $cm^{-1}$ (left) and above 450 $cm^{-1}$ (right). Each color corresponds to an assigned symmetry: green ($A_u$), red ($B_{1u}$), black ($B_{2u}$) and blue ($B_{3u}$). Dashed lines indicate the pressures at which changes in the slopes of vibrational modes are observed. Note the change of slope of several modes around 2, 4 and 10 GPa.

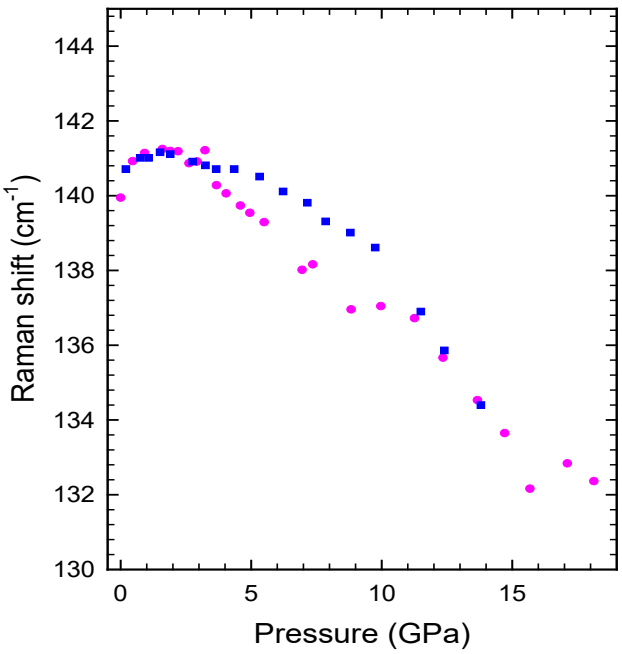


**Figure S25**. Detail of the pressure dependence of the experimental Raman-active mode near 140 $cm^{-1}$ obtained from powder (circles) and single-crystal (squares) samples. A change in slope is observed close to 2 GPa in agreement with the change in compressibility of the internal structures of valentinite.

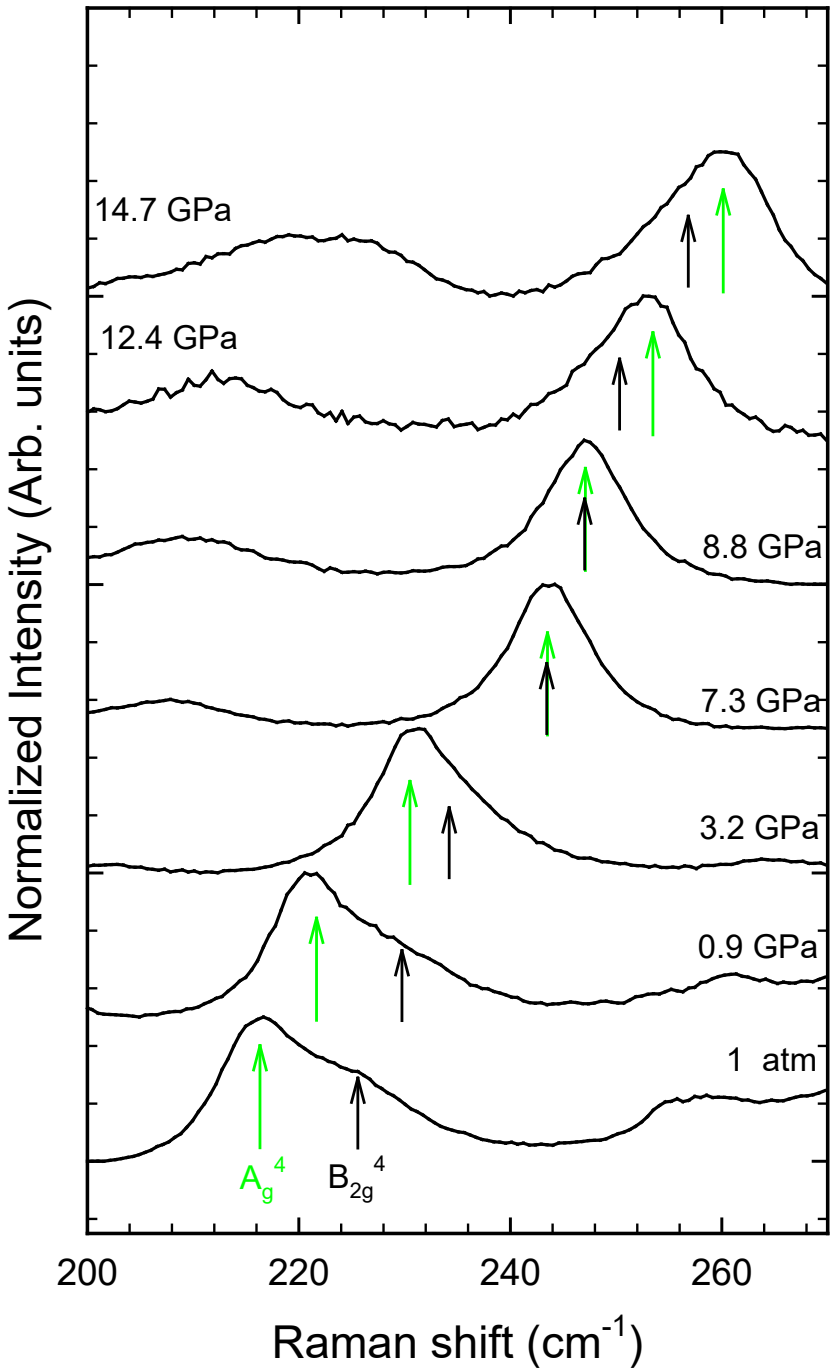


**Figure S26.** Detail of the pressure dependence of the Raman shift of the $B_{2g}^4$ and $A_g^4$ modes.

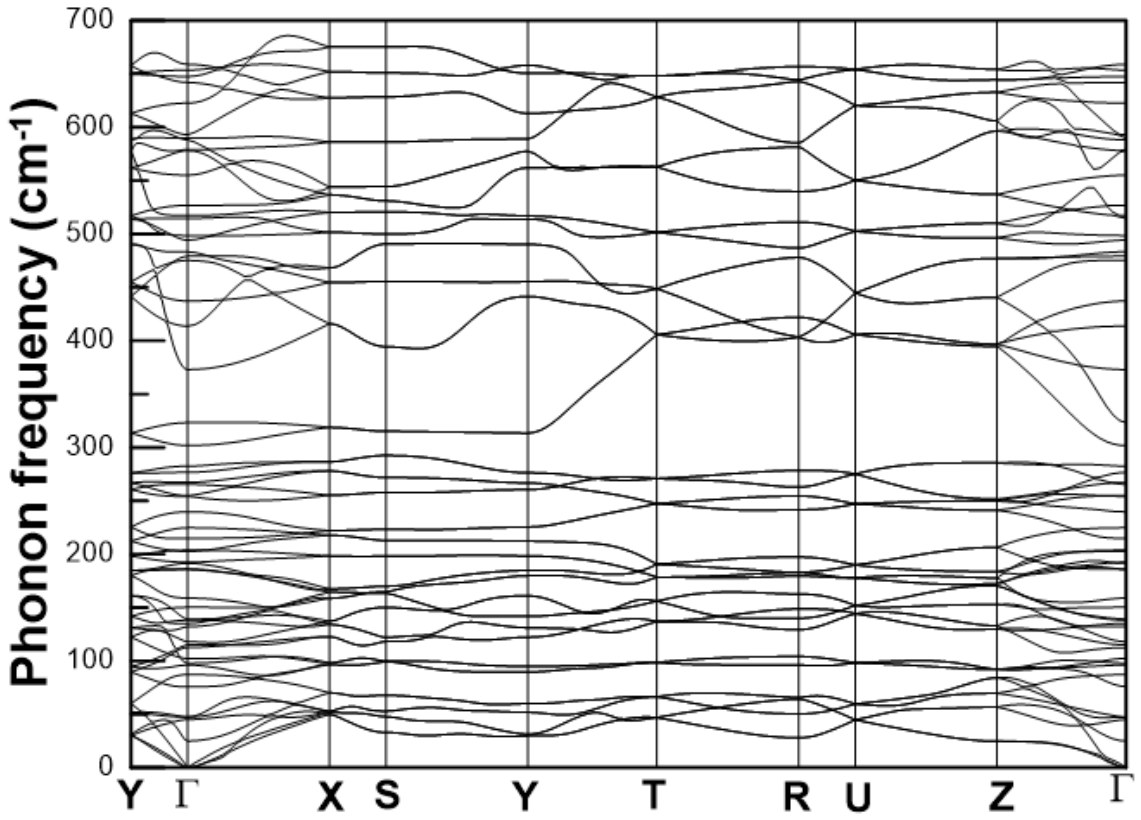


**Figure S27**. Phonon dispersion curve of β-$Sb_2O_3$ obtained by *ab-initio* theoretical calculations at 0 GPa. No soft phonon has been observed in β-$Sb_2O_3$ up to 15 GPa.

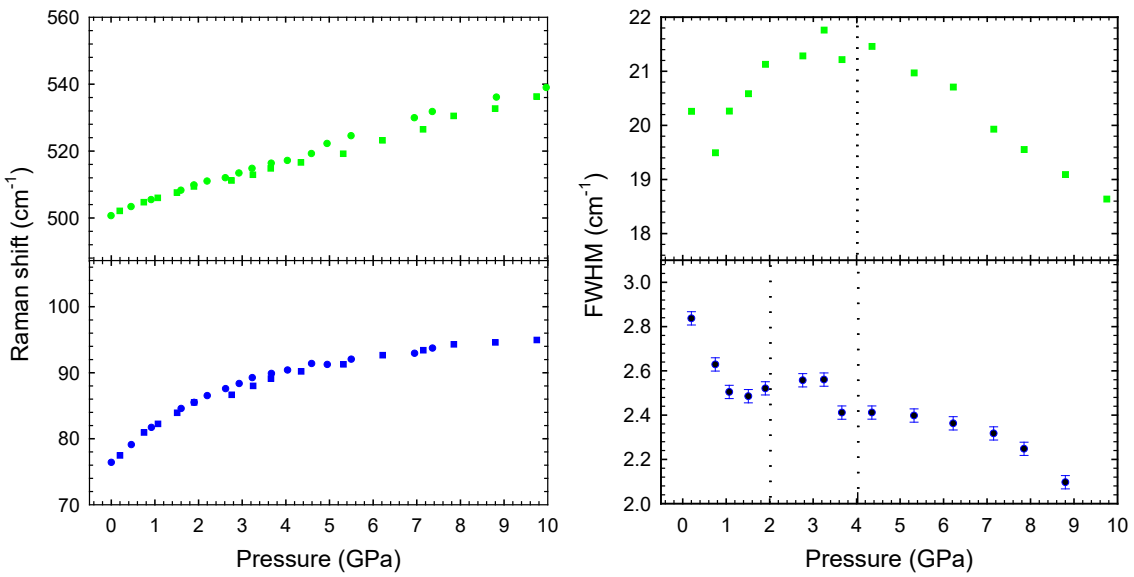


**Figure S28.** Detail of the pressure dependence of the experimental Raman-active mode frequencies (left) and their corresponding linewidths (right) for the modes near 80 ($B_{2g}^{1}$) and 500 $cm^{-1}$ ($A_g^6$)) in powder (circles) and single-crystal (squares) β-$Sb_2O_3$. A change in the slope of the FWHM is observed at 2 and 4 GPa in the low-frequency mode and at 4 GPa in the high-frequency mode.

**Table S4.** Experimental and theoretical frequencies and pressure coefficients of Raman-active modes in valentinite below 2 GPa. Our values are compared to those of Geng et al. **[17]**.

| Mode | Experimental | | Theoretical | | Geng et al.[15] | |
|---|---|---|---|---|---|---|
| | $\omega_0$ ($cm^{-1}$) | $a$ ($cm^{-1}$/GPa) | $\omega_0$ ($cm^{-1}$) | $a$ ($cm^{-1}$/GPa) | $\omega_0$ ($cm^{-1}$) | $a$ ($cm^{-1}$/GPa) |
| ($B^1_{2g}$) | 76.8 | 4.8(3) | 44.3 | 5.8 | | |
| ($A^1_g$) | | | 75.8 | 1.6 | | |
| ($B^1_{3g}$) | | | 87.6 | 2.4 | | |
| ($B^2_{2g}$) | 106.1 | 1.0(2) | 102.7 | 1.8 | 104 | - |
| ($B^2_{3g}$) | | | 112.7 | 1.7 | 115 | 0.321 |
| ($B^1_{1g}$) | | | 114.5 | 4.8 | | |
| ($B^3_{3g}$) | | | 130.2 | 1.2 | | |
| ($A^2_g$) | | | 133.5 | -0.90 | | |
| ($B^2_{1g}$) | 139.8 | 0.8(1) | 138.1 | 0.63 | 139 | -0.475 |
| ($B^3_{2g}$) | | | 150.1 | 3.5 | | |
| ($B^4_{3g}$) | | | 159.1 | 5.4 | 192 | 1.639 |
| ($A^3_g$) | | | 191.6 | 3.6 | | |
| ($B^3_{1g}$) | 187.2 | 4.8(1) | 192.6 | 2.6 | 223 | 2.155 |
| ($A^4_g$) | 218.7 | 3.6(1) | 215.3 | 6.0 | | |
| ($B^4_{2g}$) | 224.5 | 3.5(1) | 224.8 | 3.7 | | |
| ($B^5_{3g}$) | 258.0 | 2.2(1) | 254.2 | 2.9 | 259 | 0.672 |
| ($B^4_{1g}$) | | | 266.5 | 2.7 | | |
| ($B^5_{2g}$) | 283.3 | 1.9(1) | 276.1 | 2.6 | | |
| ($A^5_g$) | 294.7 | 2.0(1) | 301.2 | 2.7 | 293 | 1.770 |
| ($B^5_{1g}$) | 443.7 | 5.0(1) | 436.4 | 5.2 | | |
| ($B^6_{2g}$) | | | 478.8 | 1.1 | 449 | 2.499 |
| ($B^6_{3g}$) | 487.6 | 2.6(2) | 483.7 | 2.8 | 491 | 0.977 |
| ($A^6_g$) | 500.9 | 4.7(1) | 498.4 | 4.2 | 506 | 3.579 |
| ($B^6_{1g}$) | | | 526.7 | 6.9 | | |
| ($B^7_{2g}$) | | | 578.2 | 3.4 | | |
| ($B^7_{3g}$) | | | 589.5 | 8.2 | | |
| ($A^7_g$) | 595.8 | 9.6(2) | 589.0 | 8.4 | | |
| ($B^8_{2g}$) | | | 647.1 | 4.1 | 608 | 4.660 |
| ($B^7_{1g}$) | | | 653.5 | 5.7 | 684 | 3.548 |
| ($B^8_{3g}$) | 683.3 | 2.9(1) | 658.9 | 0.52 | | |

**Table S5.** Experimental and theoretical frequencies and pressure coefficients of Raman-active modes in valentinite between 2 and 10 GPa. Our values are compared to those of Geng et al.**[17]**.

| Mode | Experimental | | Theoretical | | Geng et al. **[17]** | |
|---|---|---|---|---|---|---|
| | $\omega_2$ ($cm^{-1}$) | $a$ ($cm^{-1}$/GPa) | $\omega_2$ ($cm^{-1}$) | $a$ ($cm^{-1}$/GPa) | $\omega_2$ ($cm^{-1}$) | $A$ ($cm^{-1}$/GPa) |
| ($B^1_{2g}$) | 83.3 | 1.7(1) | 55.9 | 3.1 | | |
| ($A^1_g$) | | 0.6(3) | 79.0 | 0.5 | | |
| ($B^1_{3g}$) | | | 92.4 | 0.1 | | |
| ($B^2_{2g}$) | 108.1 | 1.0(2) | 106.3 | 2.3 | 104 | - |
| ($B^2_{3g}$) | | -0.2(1) | 116.1 | 1.0 | 115 | 0.321 |
| ($B^1_{1g}$) | | 6.1(18) | 124.1 | 2.6 | | |
| ($B^3_{3g}$) | | | 132.6 | 2.3 | | |
| ($A^2_g$) | | | 131.7 | 0.3 | | |
| ($B^2_{1g}$) | 141.1 | -0.53(5) | 139.4 | 1.0 | 139 | -0.475 |
| ($B^3_{2g}$) | | 1.8(1) | 157.1 | 2.7 | | |
| ($B^4_{3g}$) | | | 169.9 | 4.3 | 192 | 1.639 |
| ($A^3_g$) | | | 198.8 | 2.8 | | |
| ($B^3_{1g}$) | 198.0 | 1.7(1) | 197.8 | 2.2 | 223 | 2.155 |
| ($A^4_g$) | 225.0 | 3.2(3) | 227.3 | 4.3 | | |
| ($B^4_{2g}$) | 231.5 | 3.5(1) | 232.2 | 2.4 | | |
| ($B^5_{3g}$) | 262.4 | 1.2(1) | 260.0 | 2.2 | 259 | 0.672 |
| ($B^4_{1g}$) | | | 271.9 | 3.2 | | |
| ($B^5_{2g}$) | 287.1 | 2.1(1) | 281.3 | 3.7 | | |
| ($A^5_g$) | 298.7 | 2.1(1) | 306.6 | 2.9 | 293 | 1.770 |
| ($B^5_{1g}$) | 453.7 | 3.9(1) | 446.8 | 5.2 | | |
| ($B^6_{2g}$) | | | 481.0 | 1.3 | 449 | 2.499 |
| ($B^6_{3g}$) | 492.8 | 1.5(2) | 489.3 | 1.9 | 491 | 0.977 |
| ($A^6_g$) | 510.3 | 3.5(1) | 506.8 | 3.1 | 506 | 3.579 |
| ($B^6_{1g}$) | | | 540.5 | 5.8 | | |
| ($B^7_{2g}$) | | | 585.0 | 3.0 | | |
| ($B^7_{3g}$) | | | 605.9 | 4.4 | | |
| ($A^7_g$) | 615.0 | 6.6(1) | 605.8 | 5.9 | | |
| ($B^8_{2g}$) | | | 655.3 | 4.5 | 608 | 4.660 |
| ($B^7_{1g}$) | | | 664.9 | 4.9 | 684 | 3.548 |
| ($B^8_{3g}$) | 689.1 | 4.5(1) | 659.9 | 2.2 | | |

**Table S6.** Theoretical frequencies and pressures coefficients of IR-active and silent (inactive) modes in valentinite. Experimental mode frequencies of IR-active modes at room pressure from literature are given for comparison.

| Mode | Theoretical* | | Theoretical** | | Experimental |
|---|---|---|---|---|---|
| | $\omega_0$ ($cm^{-1}$) | $a$ ($cm^{-1}$/GPa) | $\omega_0$ ($cm^{-1}$) | $a$ ($cm^{-1}$/GPa) | $\omega_0$ ($cm^{-1}$) |
| ($B^1_{2u}$) | 24.7 | 4.5(1) | 33.7 | 2.0(1) | |
| ($A^1_u$) | 45.5 | 2.2(4) | 49.9 | 2.3(1) | |
| ($B^1_{3u}$) | 47.2 | 1.9(2) | 51.0 | 2.5(2) | |
| ($A^2_u$) | 95.9 | -1.2(1) | 93.5 | 0.7(1) | |
| ($B^2_{2u}$) | 97.8 | 0.4(5) | 98.6 | 2.3(1) | |
| ($B^2_{3u}$) | 117.2 | 1.8(5) | 120.8 | 3.2(3) | |
| ($B^1_{1u}$) | 138.7 | 2.3(4) | 14303 | 1.9(1) | |
| ($B^2_{1u}$) | 185.2 | 4.3(3) | 193.8 | 2.9(2) | |
| ($B^3_{2u}$) | 185.8 | 3.7(3) | 193.2 | 2.1(1) | |
| ($B^3_{3u}$) | 202.7 | 3.0(1) | 208.7 | 2.5(1) | |
| ($A^3_u$) | 203.9 | 2.8(1) | 209.5 | 1.8(1) | |
| ($B^3_{1u}$) | 239.0 | 4.6(2) | 248.2 | 3.2(3) | |
| ($A^4_u$) | 254.2 | 1.6(1) | 257.4 | 2.0(1) | |
| ($B^4_{2u}$) | 265.2 | 2.9(2) | 271.0 | 2.1(1) | |
| ($B^4_{3u}$) | 282.4 | 2.7(1) | 287.8 | 2.3(1) | 280[c] |
| ($B^4_{1u}$) | 322.8 | 2.2(2) | 327.2 | 2.3(1) | |
| ($B^5_{2u}$) | 372.9 | -0.2(1) | 372.5 | 1.2(1) | 385[c] |
| ($B^5_{3u}$) | 413.6 | 0.9(4) | 415.4 | 1.8(1) | |
| ($A^5_u$) | 474.7 | 6.7(2) | 488.1 | 5.1(4) | 455[a,b],440[c] |
| ($A^6_u$) | 494.4 | 8.0(2) | 510.4 | 6.4(4) | 488[b,c] |
| ($B^5_{1u}$) | 514.1 | 3.1(1) | 520.3 | 3.3(3) | |
| ($B^6_{2u}$) | 516.5 | 4.3(1) | 525.1 | 4.4(3) | |
| ($B^6_{3u}$) | 555.1 | 1.9(1) | 558.9 | 1.3(1) | 540-545[a,b,c] |
| ($B^6_{1u}$) | 578.5 | 9.3(2) | 597.1 | 5.6(4) | |
| ($A^7_u$) | 592.8 | -0.4(1) | 592 | 0.7(1) | 585-589[a,b,c] |
| ($B^7_{3u}$) | 622.4 | 1.2(1) | 624.8 | 2.5(2) | |
| ($B^7_{2u}$) | 642.2 | 3.5(3) | 649.2 | 3.1(2) | 685[a], 688[c],720[c], 740[b] |

* below 2 GPa, ** between 2 and 10 GPa, [a] Ref. [21], [b] Ref. [18], [c] Refs. [16]

**Electronic band structure of valentinite around 10 GPa**

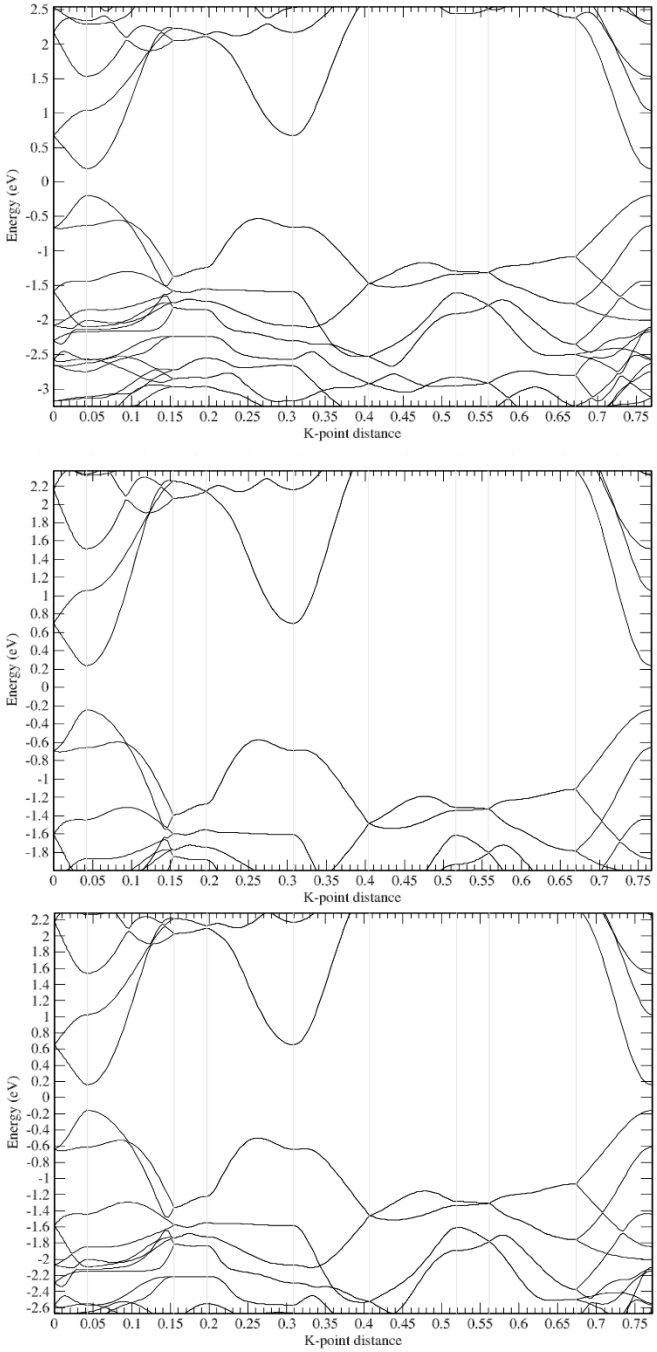


**Figure S29**. Detail of the electronic band structure of β-$Sb_2O_3$ near the bandgap region at 9.5 GPa (top), at 10.5 GPa (middle) and at 11.3 GPa (bottom).

**References**


1. R. M. Bozorth, The Crystal Structures of the Cubic Forms of Arsenious and Antimonous Oxides. *J. Amer. Chem. Soc.,* 1923, **45**, 1621.

2. M. J. Buerger, S. B. Hendricks, S.B. The Crystal Structure of Valentinite (Orthorhombic $Sb_2O_3$[1]). *Z. Krist., 1938,* **98**, 1.

3. D. Orosel, R. E. Dinnebier, V. A. Blatov, M. Jansen. Structure of a new high-pressure–high-temperature modification of antimony(III) oxide, c-$Sb_2O_3$, from high-resolution synchrotron powder diffraction data. *Acta Crystallographica Section B,* 2012, **68**, 1.

4. M. Li, F. Li, P. G. Yin, Tailoring the Band Structure of β-$Bi_2O_3$ by co-Doping for Realized Photocatalytic Hydrogen Generation. *Chem. Phys. Lett.*, 2014, **601**, 92.

5. A. L. J. Pereira, J. A. Sans, R. Vilaplana, O. Gomis, F. J. Manjón, P. Rodríguez-Hernández, A. Muñoz, C. Popescu and A. Beltrán, Isostructural Second-Order Phase Transition of β-Bi2O3 at High Pressures: An Experimental and Theoretical Study, *J. Phys. Chem. C,* 2014, **118**, 23189.

6. A. L. J. Pereira, O. Gomis, J. A. Sans, J. Contreras-García, F. J. Manjón, P. Rodríguez-Hernández, A. Muñoz, A. Beltrán, β−Bi2O3 under compression: Optical and elastic properties and electron density topology analysis, *Phys. Rev. B,* 2016, **93**, 224111.

7. A.-H. Geng, L.-H. Cao, Y.-M. Ma, Q.-L. Cui, C.-M. Wan, Experimental Observation of Phase Transition in Sb2O3 under High Pressure, *Chin. Phys. Lett.*, 2016, **33**, 097401.

8. I. R. Beattie, K. M. S. Livingston, G. A. Ozin, D. J. Reynolds, Single-crystal Raman Spectra of Arsenolite ($As_4O_6$) and Senarmonite ($Sb_4O_6$). The Gas-phase Raman Spectra of $P_4O_6$, $P_4O_{10}$, and $As_4O_6$. *J. Chem. Soc. A*, 1970, **0**, 449.

9. G. Mestl, P. Ruiz, B. Delmon, H. Knozinger, $Sb_2O_3$/$Sb_2O_4$ in Reducing/Oxidizing Environments: An in Situ Raman Spectroscopy Study. *J. Phys. Chem.*, 1994, **98**, 11276.

10. S. J. Gilliam, J. O. Jensen, A. Banerjee, D. Zeroka, S. J. Kirkby, C. N. Merrow, A theoretical and experimental study of $Sb_4O_6$: vibrational analysis, infrared, and Raman spectra. *Spectrochimica Acta Part A*, 2004, **60**, 425.

11. A. L. J. Pereira, L. Gracia, D. Santamaría-Perez, R. Vilaplana, F. J. Manjon, D. Errandonea, M. Nalin, A. Beltrán, Structural and vibrational study of cubic Sb2O3 under high pressure, *Phys. Rev. B,* 2012, **85**, 174108.

12. B. S. Naidu, M. Pandey, V. Sudarsan, R. K. Vatsa, R. Tewari, Photoluminescence and Raman spectroscopic investigations of morphology assisted effects in $Sb_2O_3$. *Chem. Phys. Lett.,* 2009, **474**, 180.

13. A. E. Panasenko, L. A. Zemnukhova, L. N. Ignatieva, T. A. Kaidalova, S. I. Kuznetsov, N. V. Polyakova, Y. V. Marchenko, Phase composition of antimony(III) oxide samples of different origin, *Inorg. Mater.,* 2009, **45**, 402.

14. Z. Deng, F. Tang, D. Chen, X. Meng, L. Cao, B. Zou, A Simple Solution Route to Single-Crystalline $Sb_2O_3$ Nanowires with Rectangular Cross Sections. *J. Phys. Chem. B*, 2006, **110**, 18225.

15. P. J. Miller, C. A. Cody, Infrared and Raman investigation of vitreous antimony trioxide, *Spectrochim. Acta A,* 1982, **38**, 555.

16. C. A. Cody, L. Dicarlo, R. K. Darlington, Vibrational and thermal study of antimony oxides, *Inorg. Chem.*, 1979, **18**, 1572.

17. A.-H. Geng, L. Cao, C. Wan, Y. Ma, High-pressure Raman investigation of the semiconductor antimony oxide, *Phys. Stat. Sol. C*, 2011, **8**, 1708.

18. E. I. Voit, A. E. Panasenko, L. A. Zemnukhova, Vibrational spectroscopic and quantum chemical study of antimony(III) oxide, *J. Struct. Chem.,* 2009, **50**, 60.

19. M. I. Arroyo, J. M. Perez-Mato, C. Capillas, E. Kroumova, S. Ivantchev, G. Madariaga, A. Kirov, H. Wondratschek, Bilbao Crystallographic Server I: Databases and crystallographic computing programs, *Zeitschrift für Kristallographie,* 2006, **221**, 15.

20. P. Canepa, R. M. Hanson, P. Ugliengo, M. Alfredsson, J-ICE: A New Jmol Interface for Handling and Visualizing Crystallographic and Electronic Properties. *J. Appl. Crystallogr.*, 2011, **44**, 225.

21. Z. M. Hanafi, K. A. Alzewel, E. M. H. Ibrahim, M. M. Abou Sekkina, Physico-Chemical Properties of $M_2^{VB}$ $N_3^{VIB}$ Compounds. *Z. Phys. Chem.,* 1975, **94S**, 291.